united nations
educational, scientific
and cultural
organization

international atomic
energy agency

the
abdus salam
international centre for theoretical physics

SMR/1328/18

School on the Physics of Equatorial Atmosphere

(24 September - 5 October 2001)

Small Scale structure of the ionosphere and effects: Instabilities, Spread F depletions etc.

M. A. Abdu
(Instituto Nacional de Pesquisas Espaciais, São José dos Campos, Brazil)

Small-scale structures of the ionosphere and effects: Instabilities, Spread F depletions etc. (M. A. Abdu)

1-Introduction:

Ionospheric structures are manifestations of the diverse processes (physical, dynamical, electrodynamical, and chemical processes) that control the ionospheric current and density distributions. Large scale structures are those associated with large distances and slow changes in time, such as, vertical layer structure measures in tens and hundreds of kilometers, day-to-night variations, longitude & latitude variations involving hundreds to thousands of kilometers and so on. Investigations of such structures require large number of observing systems at a time.

On the other hand smaller scale structures go down to kilometer and to meter sizes small enough to be diagnosed by a single observing instruments (or observing systems restricted to a specific location. They can be produced by the following processes: 1- Atmospheric gravity waves in the E and F layers (of a few kilometers- 100s of kilometers), 2- Plasma instability mechanism, working on electric fields, winds and density gradients (at meter sizes to 100s of kilometer sizes), and 3- Atmospheric turbulence.

The small-scale structures can occur in a wide range of altitude extending from D region to the topside F region. The structures produced by plasma instability mechanism, which we will be focusing here extend upward from the base of the E region (~ 95 km).

2- Basic measurement techniques

Depending upon the scale sizes of the structures different diagnostic techniques need to be employed to study them. The main techniques used are outlined in the following table:

Technique of measurement	Structure sizes
Digital ionosondes, HF Doppler radars	100s of meters to a few kilometers; extending to 100s of kilometers for oblique echoes
Scintillation receivers on satellite beacons	10s of meters to kilometer sizes
TEC	Few km to 100s of km
VHF/UHF radars	10s of centimeters to a few meters
Satellite born in situ sensors	~1m to larger sizes (~1000 km) in mostly horizontal distribution
Rocket based in situ sensors	~1m to all larger sizes ~(100 km)in mostly vertical distribution
Airglow imagers and scanning photometers	10s to 100s of kilometers

The earliest observation of the ionospheric structure signature was detected by vertical sounding ionograms taken over Huancayo in Peru situated over the magnetic

equator. Subsequently, various techniques were employed for investigating ionospheric irregularities. The most widely used are the following techniques: HF fading with spaced receiver technique, scintillation of trans- ionospheric satellites beacons, HF Doppler radars, coherent back-scatter radar at VHF, satellites in situ measurements, rocket in situ measurement and optical imaging and photometry of night air-glow. **Fig. 1** shows the scale sizes distribution and the corresponding diagnostic techniques widely utilized to investigate them.

Some examples of structure signatures as diagnosed by these instruments are shown in the following figures: (**Figs2 a, b, c** etc.)

Drift measurements of the structures

The structures are highly dynamic, being driven by electric field or neutral wind depending upon the height at which they occur. In the D and lower E region the irregularities are diagnosed by partial reflection of the radio waves in the medium – high frequency band (usually 2-6 MHz). The velocity of the structures represents that of the neutral wind. From approximately 95 km upward the drift velocity is a measure of the electric field that drive them.

The methods used to study the structure velocities are the following:

1-Relatively simple method to measure horizontal movements based on spaced receiver technique,

2- More sophisticated techniques based measurement of Doppler frequency spectrum by VHF/UHF coherent backscatter radars and HF radars to determine the three components of the velocity vector and the intensity distribution with height/range of the structures.

3- Optical techniques based on imaging and angular scanning measurements of airglow emission modulated by varying electron densities of the structures.

Method –1:
The method (1) of measuring the irregularity velocity is based on: 1- the fading of HF signals, from ground based transmitters, reflected by the ionospheric structures, and 2- scintillation of radio beacons from satellites received on the ground. In both cases signals are recorded by receivers spaced by 10s to a few 100s of meters making sure that the fading patterns at the receivers are correlated.
The method of determining velocity for the case (1) of fading signals reflected by the structures is illustrated in **Fig.3**. If the spacing of the receivers is smaller than the correlation distance of fading then each receiver will record similar fading pattern as shown in (a). These patterns are produced by the horizontal movement on the ground of a diffraction pattern produced by the structures. Knowing the separation of the receivers it is possible to deduce the speed and direction of motion as follows:

$$V_x' = R_1 R_3 / t_2$$
$$V_x' = R_1 R_2 / t_1$$
The velocity, V, of the fading front is given by,
$$1/V^2 = 1/(V_x')^2 + 1/(V_y')^2 ,$$

and hence
$V = (V_x' V_y')/ [(V_x')^2 + (V_y')^2]^{1/2}$,
Also,
$\theta = \tan^{-1}(V_x'/V_y')$

The horizontal velocity so obtained is 2 times the velocity of the structures producing the diffraction pattern.

If the pattern changes as it moves the time difference recorded will be smaller, and the true velocity will be smaller than the measured velocities in this case. (see, for more details, Hargreaves, The solar-terrestrial environment, Cambridge, 1992). Movements at the reflection points can be studied by transmitting a signal from the ground.

For the case (2) based on scintillation of satellite beacon signals, the geometry is shown in **Fig.4**. In this case also three or more receivers can be used for recording scintillation on the received signals. This system is sensitive to the integrated effect of the irregularities distributed in height along the ray path. The apparent speed of the irregularities over ground (V_g) depends upon the satellite velocity (V_s) and the effective height (h_i) of the irregularities as a fraction of the satellite altitude (h_s), so that:

$$V_{g,} = V_{,s}\, h_i /(h_{s,} - h_i).$$
And
$$h_{,i} = h_s/(1 + V_s/V_g).$$

These heights fall in the range of 200- 600 km with maximum around 300-400 km.

Method-2:

The method (2) uses coherent echoes scattered by structures having the scale sizes half radar wave length. For example radar at 50 MHz (many VHF radars are operated at this frequency) detects structures of 3m size. The geometry of observing theses structures is shown in **Fig. 5**.
A simplified scheme of a VHF coherent back-scatter radar such as that are operated at Jicamarca, Peru, Thumba India, and Sao Luis, Brazil is shown in Fig. (to be included).

The method –3: will be briefly discussed later.

3- Structures arising from plasma instability processes

The basic driving forces for the instability processes are:
- Electric fields from a- Ionospheric dynamo,
- b- Magnetospheric dynamo
- Neutral winds and waves
- Density gradients
- Gravity field.

The instability processes basically involve plasma drift and electric currents. Under quiet conditions the basic E-field originate from ionospheric dynamo resulting from winds blowing blowing perpendicular to earth's magnetic field. Such conditions are

best met at equatorial and auroral/polar regions, and therefore plasma structures due to instability processes occur more efficiently at these latitudinal zones of the earth where the geomagnetic field lines are horizontal and nearly vertical respectively.

Over high latitudes much of the instability process are associated with magnetospheric dynamo electric field, and density enhancements are and gradients produced by precipitation of energetic particles, during magnetic storms. Under such conditions electric fields do penetrate to equatorial latitudes where they control the plasma instability processes, which will be discussed separately.

Plasma structure of the equatorial ionosphere:

Equatorial electrojet instabilities:

The large vertical Hall electric field (E_z) in the E region over the dip equator is responsible for driving the electrojet current system and associated instabilities.

$$E_z = (1 + \sigma_H/\sigma_p)\, Ex$$

Written also as:

$$E_z = \frac{\nu_i}{\Omega_i}\left[\frac{E_x}{1+\frac{\nu_i\nu_e}{\Omega\,\Omega_{ei}}}\right] = \frac{1}{k_i}\frac{E_x}{1+\psi_0} \qquad 1$$

Subtituting standard values for k_i and ψ_0 Eq.1 shows that E_z is of the order of 20-30 times E_x (that is, 10 – 15 mV/m). The elctrons are magnetized and under this electric field which is vertically upward they drift westward with a velocity that can reach of the order of 400-600 m/s.

There are two situations under which plasma instability can be produced:

1- The electron flow velocity (V_e) can turn supersonic exceeding the ion-acoustic speed (C_s), that is, Ve > C_s. Such a situation could become unstable to meter size electrostatic waves, leading to the generation of the two-stream instability.
2- The condition when E_z is parallel to the zero order (ambient) electron density gradient favors generation of gradient drift instability.

Further details on these mechanisms will be discussed later.

The plasma structures produced by these instabilities in the EEJ extend from meter to kilometer sizes that scatter radio wave in the HF to VHF frequency ranges.

The occurrence of an anomalous scattering layer in the E layer close to the dip equator was initially observed by ionosonde. The corresponding ionogram traces resemble that produced by a sporadic E layer and hence this trace was named E_{sq} "Equatorial Sporadic E layer". Its association with the EEJ current was confirmed from:

1- The intensity of the layer was correlated with electrojet strength as seen in magnetograms.
2- VHF forward scattering experiment showed the echoes to be field aligned and caused by electron density irregularities immersed in electrojet.

Most important early results on the physics of these irregularities have been obtained from the VHF radar measurements performed over Jicamarca Radio Observatory. This was continued and followed by Rocket observations from Thumba (India), Punta Lobo (Peru), Kwajelein Island (Pacific) and VHF radar observations in Central Africa and India, that have contributed to a better understanding of the EEJ irregularity processes.

Other known characteristics of these structures are:
-They is field aligned so that their wave number along the magnetic field ($k_{||}$) is much less than $k_{\perp}$?
-The radar echoes are observed only when the wave vector is nearly perpendicular to the earth's magnetic field, the aspect sensitivity is within ~1°

Ionosonde diagnostic of E_{sq} structures.

Fig. 6,(a) shows an example with normal E layer and (b,c,d) with E_{sq} trace near 100 km in the ionogram. The slant trace of the E_{sq} is produced by the increasing cone of reception of the signal scattered by the irregularities as a result of the increasing frequency penetrating at increasingly slant angle into the irregularity layer as illustrated in **Fig.7**. Such characteristics of the trace shows that E_{sq} structures produced by instability processes occur at the positive density gradient region of the E layer and the association with the EEJ strength showed that the vertical Hall electric field was pointing upward in the direction of the density gradient.

Radar diagnostics of the EEJ structures

Most of the investigations have been done using coherent backscatter radars at VHF sensitive to 3m size structures (corresponding to at 50 MHz radar frequency). These studies have revealed the existence of two types of irregularity structures, Type-1 and Type-2 associated with the EEJ. They are electrostatic waves.

Type-1 waves:

They are also known as two-stream waves (or two-stream irregularities) and are produced by instability that occurs when the electron streaming (drift) velocity attains or exceeds the ion-acoustic velocity, ~360m/s, in the electrojet region. The FFT (Fast Fourier Transform) processing of the Doppler shifted signals scattered by the two-stream waves present a narrow spectrum with a Doppler shift (of 120 ±20Hz) that corresponds to the ion-acoustic velocity. An example of an early measurement by the Jicamarca radar is shown in **Fig.8**. The mean Doppler shift of the peak is constant when the zenith angle was varied between 45° and 70° both to the east and west. During the day the Doppler shift is positive when the antenna is directed east, that is, the wave propagates westward. During the night the irregularity drift is eastward.

The zenith angle independent Doppler shift occurs due to the following process. The two-stream wave saturates at the ion-acoustic velocity, when the streaming electron velocity exceeds the latter. Therefore, for westward electron velocity exceeding the ion-acoustic velocity, there will be a range of directions along the antenna look angle for which the electron drift velocity line of sight component could exceed the ion-acoustic speed, but the saturation causes constant electron drift velocity at all these look angles.

Type-2 waves:

The average phase velocity of the Type-2 structures is smaller than the ion-acoustic speed and is approximately equal to the cosine of the radar elevation angle as shown by Balsley (JGR, 74, 233, 1969). Also, the spectral width is much broader than that of the type-1 and the mean Doppler shift of the Type-2 itself. **Fig.9** presents some examples of the Type-2 spectra over Jicamarca and corresponding average observed velocities (V_{obs}) plotted as a function of range /zenith angle (θ) which verifies the relationship, $V_{obs} = V_d Sin\theta$ for a unique value of V_d . This excellent agreement of the experimental drift velocity with elevation angle dependence shows that the type-2 phase velocity is proportional to the convection velocity of the electrojet structure. The type-2 echoes from the EEJ has been used to determine the EEJ irregularity drift velocity and hence the intensity of the dynamo electric field. This technique is not applicable when the type-1 echoes are present over a large range of zenith angle.

Fig.10 shows a simplified representation of the gradient drift instability mechanism responsible for producing the type-2 irregularities.

Fig.11- presents some examples of composite spectra showing components of both types of spectra, and **Figs.12a and b** shows by RTI maps the distribution as a function of height in the electrojet, and local time, the total received spectral power for some typical quiet days, over São Luis.

The characteristics of the type- 1 and type-2 structures differ in the following aspects.

	Type-1	Type-2
Threshold condition for instability to develop	Ve reaching C_s	No clear threshold condition
Scattering cross section	Increases with zenith angle	Proportional to the square of the drift velocity
Altitude dependence	Maximizes at maximum of V_e	Maximizes at a lower height (by ~3km)

(For more details, see Fejer and Kelly, Rev. Geophys. Space Phys. 18, 2, 401, 1980)

Some of the wave characteristics can be verified from the linear dispersion relation of the electrojet irregularities including both the two-stream and gradient drift types as derived by many authors. Its form as derived by Fejer et al. (JGR, 80,1313,1975, Rev. Geophys. Space Phys. 18, 401,1980) is given by the following relationships:

$$\omega_r \approx \frac{k \cdot \left(V_{oey} + \Psi_0 V_{oiy}\right)}{1+\Psi_0} \qquad (2)$$

$$\Gamma = \frac{1}{1+\Psi_0}\left\{\frac{\Psi_0}{\nu_i}\left[\left(\frac{k.V_d}{1+\Psi_0}\right)^2 - k^2 C_s^2\right] + \frac{\nu_i}{L_N \Omega_i}\frac{V_d}{1+\Psi_0}\right\} - 2\alpha N_0 \qquad (3)$$

ω_r is the oscillation frequency, and Γ is the growth rate. It is assumed that $\Gamma << \omega_r$
Where $V_d = V_{oey} - V_{oiy}$ is the mean westward (and normal to B) electron drift relative to the ions;

$C_s = [K(T_e + T_I)/m_i]^{1/2}$ is the ion-acoustic velocity;
ν_e, ν_i ,Ω_e and Ω_i are the electron and ion collision and gyro frequencies;
N_0 is the ambient electron density;
$L_N = N\,(\partial N/\partial z)^{-1}$ is the vertical electron density gradient length;
C_s is the ion-acoustic velocity;
$\Psi_0 = \nu_e\nu_i / \Omega_e\Omega_i$; for simplicity k is set to be equal to k_y (horizontal westward propagating wave)

The first two terms and the third term on the RHS of Eq.3 are two-stream and gradient drift driving term, respectively. The two-stream term dominate for short wave length and the gradient drift term for long wave length.
From Eq.3 we find that the condition for unstable waves propagating in a cone of aperture θ such that

$V_d \cos\theta = C_s (1+\Psi)$ (θ being the angle between the wave vector and y-axis).

Some of the characteristics that are predicted by theory but not observed:

1- Type –1 wave should be initially observed at large zenith angle and later on at small zenith angle, but observation shows simultaneous occurrence at all zenith angles;

2- The theory predicts the phase velocity $V_{ph} = V_d\cos\theta$ proportional to electron-ion drift velocity and cosine of the elevation angle. But observations show V_{ph} independent of V_d and θ;

3- Vertically propagating waves have been observed but not predicted by theory.

The EEJ structuring is highly variable in time, due to the fact that the basic driving electric field is sensitive to forcing from neutral atmosphere (gravity waves etc.) and to high latitude and magnetospheric processes through global electrodynamic coupling processes. Some examples of results on the RTI map and spectral features of the EEJ 3m irregularities during quiet conditions and under magnetically disturbed conditions, as obtained by the VHF radar at São Luis, Brazil are shown in Figs.11 and 12 a, b, c etc.

F region structures

Plasma structures of the F region (also field aligned) have scale sizes spanning 5 orders of magnitude, from meter sizes to 100s of kilometers. For this reason these structures affect radio wave propagation in wide ranging frequency bands from HF to UHF used in telecommunication and space application areas. The earliest manifestation of the presence of F region structures was observed through spread F traces in ionograms as mentioned before. Different diagnostic technique are used for their studies Examples of the structures diagnosed by different techniques are presented in **Figs. 2a,b, c, etc**. The composite effects observed by all the diagnostic techniques are now known by the generic name 'equatorial spread F', that is, ESF.

An example of a simultaneous measurement of a bubble event observed by Radar over Kwajelein in Pacific and in situ measurement of the ion density structures by rocket born sensors and from an AE-E satellite pass through the same bubble is shown in **Fig.13.** The meter size structures collocated with density depletions can be verified from this figure. A simultaneous rocket- radar diagnostic of a bubble event representing the first high altitude diagnostics of a bubble by rocket, conducted from Brazil(during the GUARA Campaign, La Belle, et al., Geophys. Res. Letts., 24, 1691, 1997) is shown in **Fig.14**.

From different signatures of the irregularities discussed above reveal that smaller scale structures are embedded in large structures of plasma depletions. These large density depletions evolve out of plasma instability process that develops at the bottom side of the F layer. The instability is believed to be driven by the gravitational Rayleigh-Taylor (GRT) mechanism. The post sunset F layer rises rapidly under the action of the pre reversal electric field, with bottomside density gradient getting steeper due to recombination and electrodynamic effects. Thus we have a situation similar to a heavy fluid resting on a light fluid, a condition that is favorable operation of GRT mechanism.

An illustration of how electrodynamics processes equivalent to the GRT mechanism can cause growth of plasma depleted structures is represented in **Fig.15**. F layer bottom-side density gradient is shown as a step function with density n1 above and vanishing below. g is downward, B is horizontal and into the paper. Ignoring collision we can show that the current produced by the gravity is: $\underline{J} = nM_g \times B/B^2$;The current in the x direction is given by: $J_x = nM_g/B$, since the current is in the g×B direction which is strictly horizontal. J_x depends on n (n is the electron density mentioned elsewhere also as Ne). So if there is a perturbation in plasma density there is a divergence and charges pile up at the edge of the perturbation as shown in the figure. As a result the perturbation electric field δE develop which causes $\delta E \times B$ drift of ions and electrons. The drift is upward in the region of depletion and downward in the region of enhancement. This results in larger perturbation and hence in larger δE and so on leading to instability.

(The system is stable if g and Δn are parallel, as is the case on the topside of the ionosphere where GRT instability does not develop).

From the equations of continuity and current convergence that include perturbations in density and potential of the form $n = n_o(z) + \delta n\, e^{i(\omega t - kx)}$ and $\phi = \phi' i(\omega t - kx)$ and after linearizing , the growth rate of the instability comes out to be:

$$\gamma = g/L\nu_{in}, \qquad (4)$$

where $L = n_o/(dn/dz)$

From radar measurement over Jicamarca, and from ionosonde measurements, of spread F irregularities, the validity of this growth rate has been verified with respect to the following conditions:

1- Irregularities occur at the positive gradient of the bottomside F region,
2- Lower the value of ν_{in}, that is, higher the height of the layer the more likely is the instability growth (irregularity occurrence).

Generalized GRT process:

The GRT process can be generalized to include the effect of a zonal electric field (that usually gets enhanced in the evening), and that of zonal wind on the instability growth rate. In the case of zonal electric field we note that the Pederson current is in the same direction as g×B (of the Figure 14). Thus the derivation for γ which considered only gravity can be generalized to include the effect of electric field by replacing $g/L\nu_{in}$ with $g/L\nu_{in} + E_{x0}/B$, where E_{x0} is the zonal component of the electric field positive eastward. Thus the growth rate become:

$$\gamma_{RT1} = g/L\nu_{in} + E_{x0}/BL \qquad (5)$$

The electric field also lifts the layer to a height of reduced ν_{in} thus increasing the growth rate further. When the electric field is westward then the growth rate will be reduced and the bottomside will be stabilized.

The effect of a zonal wind will be present when the layer is tilted so that Δn has a horizontal component as well. Under such a condition the growth rate becomes:

$$\gamma_{RT2} = \frac{g}{L\nu_{in}}\cos\sigma + \frac{E_{x0}}{BL}\cos\sigma + \frac{(E_z + uB)}{LB}\sin\sigma \qquad (6)$$

Thus we see that both a zonal electric field and a zonal wind can contribute to the instability growth rate. (see, Kelly, 1989). Under sufficiently large positive growth rate, that is, when γ, γ_{RT1} or $\gamma_{RT2} >> \beta$ the recombination loss rate, instability sets in.

The instability development is nonlinear, the perturbation electric field enhancing the density depletion and vice versa, causing the depletion to develop to the topside of the ionosphere. Such topside depletions, or bubbles, produce the radar plumes of signals scattered by meter size structures, first observed by Jicamarca Radar (Woodman and La Hoz, JGR, 81, 5447, 1976). An example of one of the first RTI maps of topside radar plumes obtained by Jicamrca radar is shown in **Fig.16.**

Nonlinear bubble development has been modeled by various authors. Considerable effort has gone into the computer simulation of the Rayleigh-Taylor instability. Such modeling is based on solving the set of equations in two dimension perpendicular to B, that is, in the equatorial plane. The set of equations consists of: Electron and ion continuity equations;

Electron and ion velocity equations; and
Charge continuity equations.

(See, for example, Zalisack et al., Nonlinear equatorial spread F: The effect of neutral winds and background Pederen conductivity, JGR, 67, 151, 1982).

Some example of the results of computer simulations nonlinear bubble development are shown in **Fig.17 a and b**. In the case of the simulation result b the westward tilt of the bubble top due the a zonal wind is in agreement with the tilt of the radar plumes such as that was present **Figs. 13,14 and16**.

It may be noted further that density at a given point changes only when a low-density region is advected to that height by the $\delta E \times B$ drift. Each density contours is specified by its initial height as well as density. This signifies that the degree of depletion observed inside a topside bubble would depend upon the region of the bottom-side density gradient at which the initial perturbation originated.

The steeping density gradient of the walls of a developing bubble become unstable to secondary instability processes, thereby setting of the development of a hierarchy of irregularities cascading into smaller sizes occupying a spectral range of ~5 orders of magnitude. The meter size is responsible for the observed radar plumes.

As the plasma depletion develop upward it drifts westward in the ambient plasma frame. Since the ambient plasma is drifting eastward at these times the bubbles would appear drifting slowly eastward at during development phase of a bubble when the polarization electric field inside the bubble is strong. With the further growth of the bubble upward the vertical polarization electric field can get weaker causing the bubble to drift zonally with nearly the same velocity as the ambient ionospheric plasma.

An example of eastward drifting bubble signature as observed by an airglow imager over Cachoeira Paulista in Brazil and a sketch of idealized bubble structures as inferred from UHF scintillation measurement (Groves et al., 1997, J. Geophys. Res., 32, 2047, 1997) are shown in **Figs.18a and b**

Bubbles can interfere with diverse space application systems that utilize trans-ionospheric radio wave propagation. One of the widely used applications is the use of GPS satellites for position determinations. An example of uncertainty that can occur in determining the coordinate of a GPS receiver is shown in **Fig. 19.**

Figure Captions:

Fig.1- Structure scale sizes sensitive to different techniques

Figs.2 a- Sample ionograms showing spread F.
b- Example of scintillation of satellite beacon
c- VHF radar plumes of bubbles
d- Satellite crossing through a bubble

Fig.3- The spaced receiver method for observing the movement of a pattern of irregularities over the ground (a) Typical fading pattern at stations R_1, R_2 , and R_3 . (b) Relation between true and apparent velocities.

Fig.4- Determination of the height of the irregularities from the apparent motion of a fading pattern on the ground.

Fig.5- Coherent scatter Radar antenna orientation for observing equatorial and auroral structures.

Fig.6- Some examples of Sporadic layer E_{sq} observed by Digisonde over São Luiz, Brazil. (a –no sporadic E layer is present, b,c,d – Es is present)

Fig.7- An illustration of how the slant trace and frequency depended increasing irregularity range in the ionogram.

Fig.8- A series of Doppler spectra from the equatorial electrojet irregularities at different elevation angles obtained at Jicamarca during a period of relatively strong scattering. The spectra are normalized to a fixed peak value (from Cohen and Bowles, JGR, 72, 822, 1967).

Fig.9- Some examples of type-2 spectra over Jicamarca (from Balsley, 1969)

Fig.10- A simplified representation of gradient drift mechanism in the equatorial electrojet during daytime.

Fig.11- Some examples of composite spectra (of type-1 and type-2) from the EEJ observed over São Luiz.

Fig.12a and b-Some examples of Range-Time-Intensity maps during some typical quiet days over São Luis.

Fig.13- Radar plumes of a topside bubble recorded by Altair radar with simultaneous vertical rocket plasma density profile (top) (Rino et al., JGR, 86, 2411, 1981), and simultaneous horizontal plasma density profile from AE-E satellite (bottom) (from Tsunoda et al., 1982, JGR).

Fig.14- A simultaneous rocket- radar diagnostic of a bubble event representing the first high altitude diagnostics of a bubble by rocket, conducted from Brazil(during the GUARA Campaign.

Fig.15- (a) Schematic diagram of the plasma analog of the Rayleigh- Taylor instability in the equatorial geometry. (b) Sequential sketches made from photos of the hydrodynamic Rayleigh –Taylor instability. A heavy fluid is initially supported by a light fluid.

Fig.16- Backscatter power maps of spread F irregularities over Jicamarca obtained using the digital power mapping technique.

Fig.17 (a)- Contour plots showing computer simulation of Rayleigh-_Taylor instability for a 100km size perturbation, initially of 5% magnitude, Contours are labeled in units of reciprocal cubic centimeters; b- Computer simulation including a background eastward neutral wind and finite Pedersen in the off –equatorial E region.

Fig.18a- Airglow all sky images of zonal drift plasma bubbles observed during a magnetic storm condition over Brazil, (b) A sketch of trans-equatorial bubble structures and their eastward drift as inferred from UHF scintillation measurements.

Fig.19- An example of position determination for a GPS receiver in the presence of Bubble associated structures. The scatter of point is due to the presence of bubbles in the trans-ionospheric propagation path.

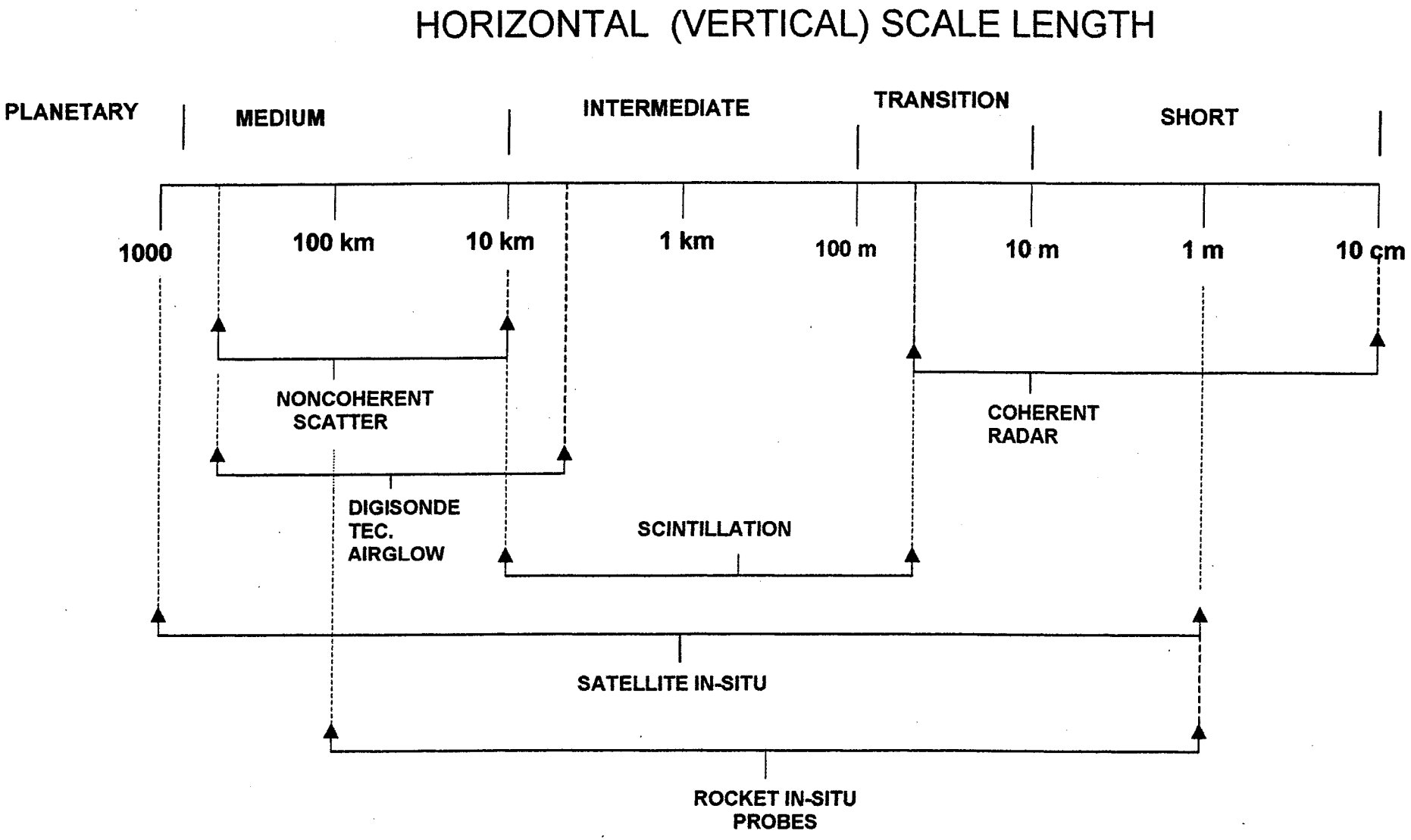
HORIZONTAL (VERTICAL) SCALE LENGTH
PLANETARY
MEDIUM
INTERMEDIATE
TRANSITION
SHORT
1000
100 km
10 km
1 km
100 m
10 m
1 m
10 cm
NONCOHERENT SCATTER
COHERENT RADAR
DIGISONDE
TEC.
AIRGLOW
SCINTILLATION
SATELLITE IN-SITU
ROCKET IN-SITU PROBES

FIG.1

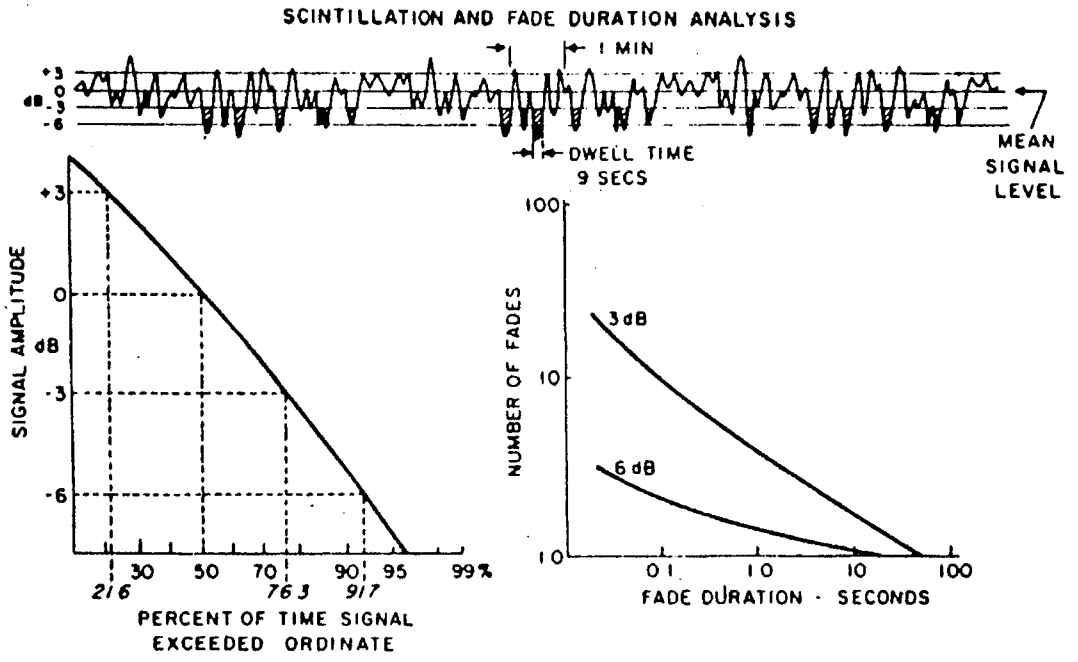

Sample of intensity fading produced by signal passing through irregularities. Fade duration and cumulative probability distribution are also shown.

Fig. 02a

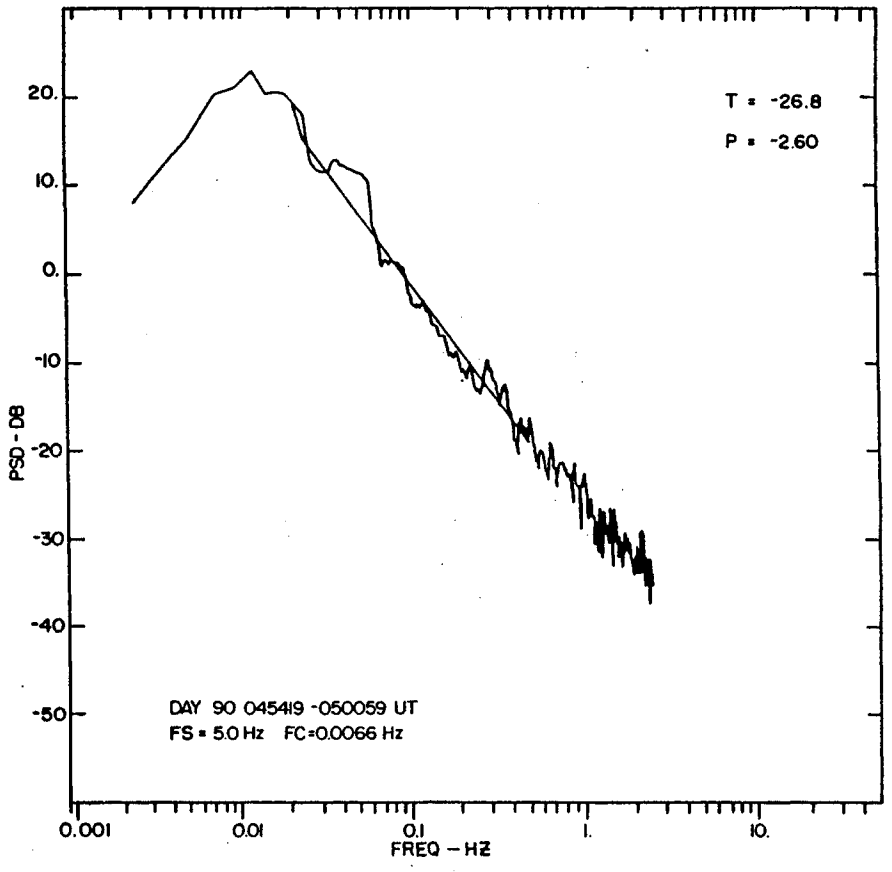
T = -26.8
P = -2.60
DAY 90 045419 -050059 UT
FS = 5.0 Hz FC=0.0066 Hz
PSD - DB
FREQ - HZ
20.
10.
0.
-10
-20
-30
-40
-50
0.001
0.01
0.1
1.
10.

a

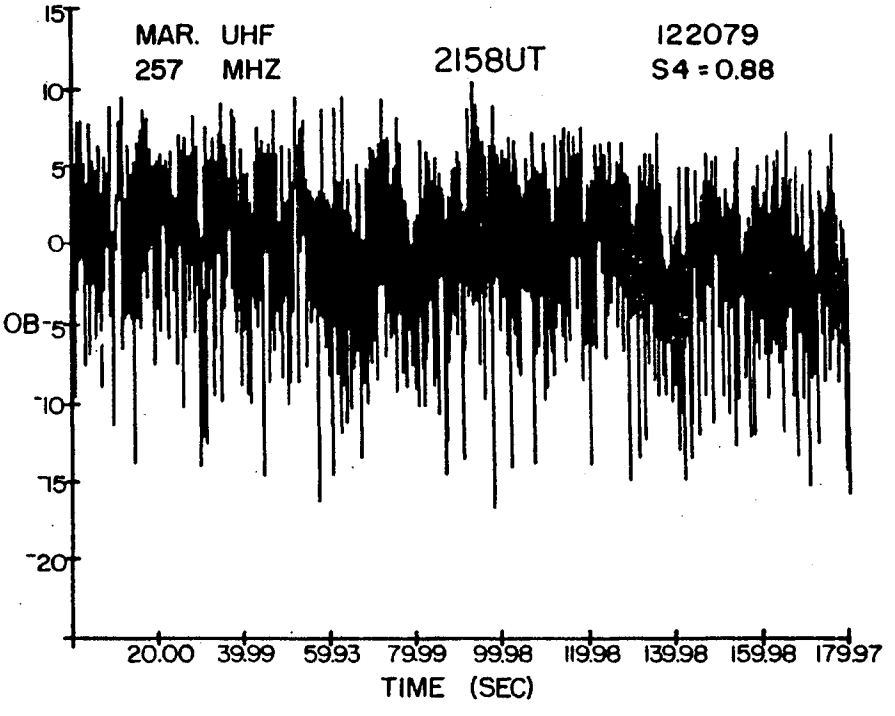
MAR. UHF
257 MHZ
2158UT
122079
S4 = 0.88
DB
TIME (SEC)
15
10
5
0
-5
-10
-15
-20
20.00
39.99
59.93
79.99
99.98
119.98
139.98
159.98
179.97

Fig. 02b

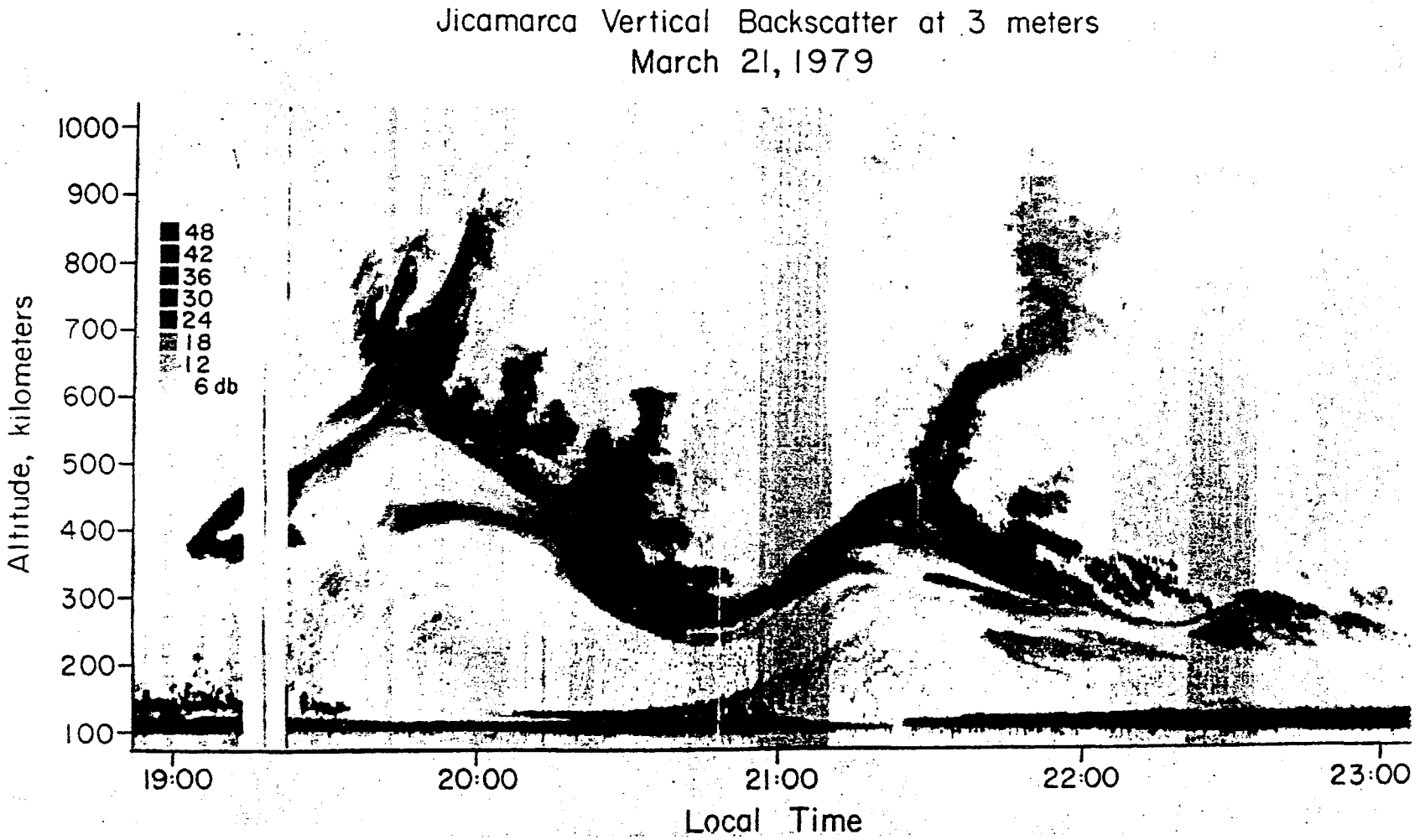

The map for March 21, 1979.

Fig. 02c

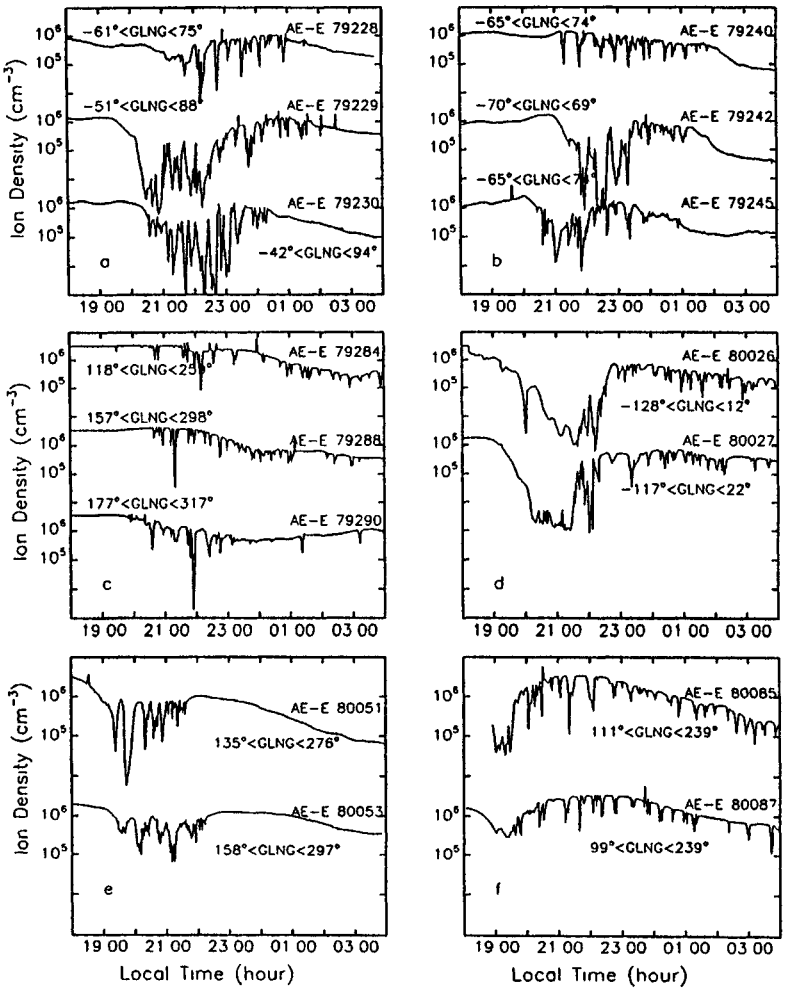

Observations on closely spaced days of similar density irregularity structures Figures 6a, 6b, and 6e show bubble structures of several hundred kilometers superimposed on the large-scale background modulations, while Figures 6c and 6f show isolated bubbles

Fig 02d

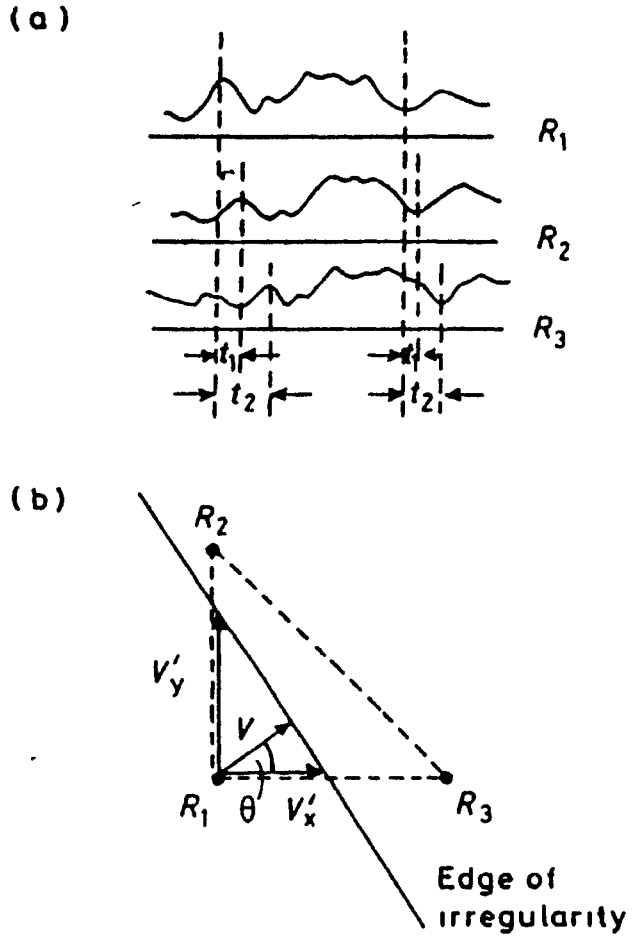

The spaced receiver method for observing the movement of a pattern of irregularities over the ground (a) Typical fading at stations R_1, R_2 and R_3 (b) Relation between true and apparent velocities

Fig 03

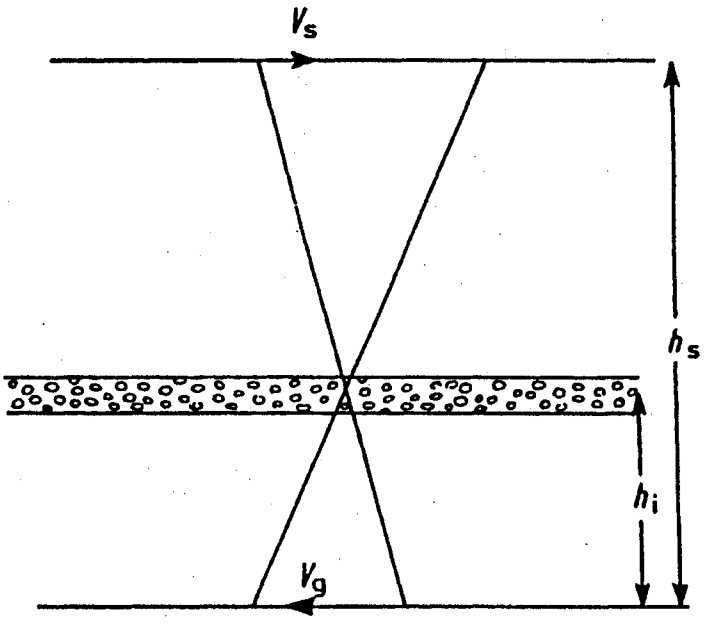

Determination of the height of irregularities from the apparent motion of a fading pattern over the ground.

Fig. 04

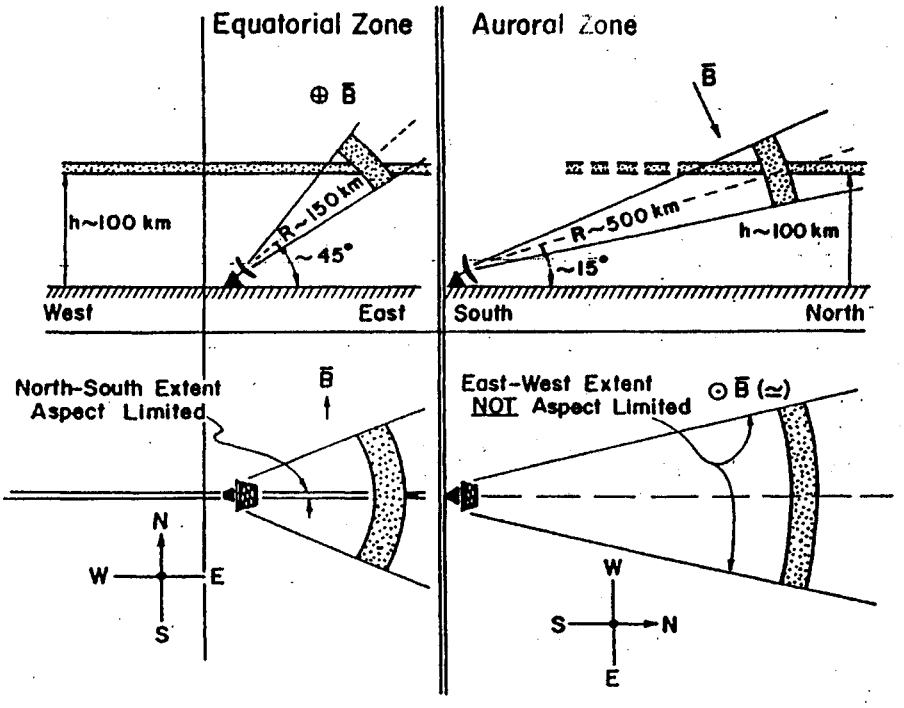

Sketch of the geometries of the *E* region equatorial (left panel) and auroral (right panel) radar experiments [after *Balsley and Ecklund,* 1972].

Fig. 05

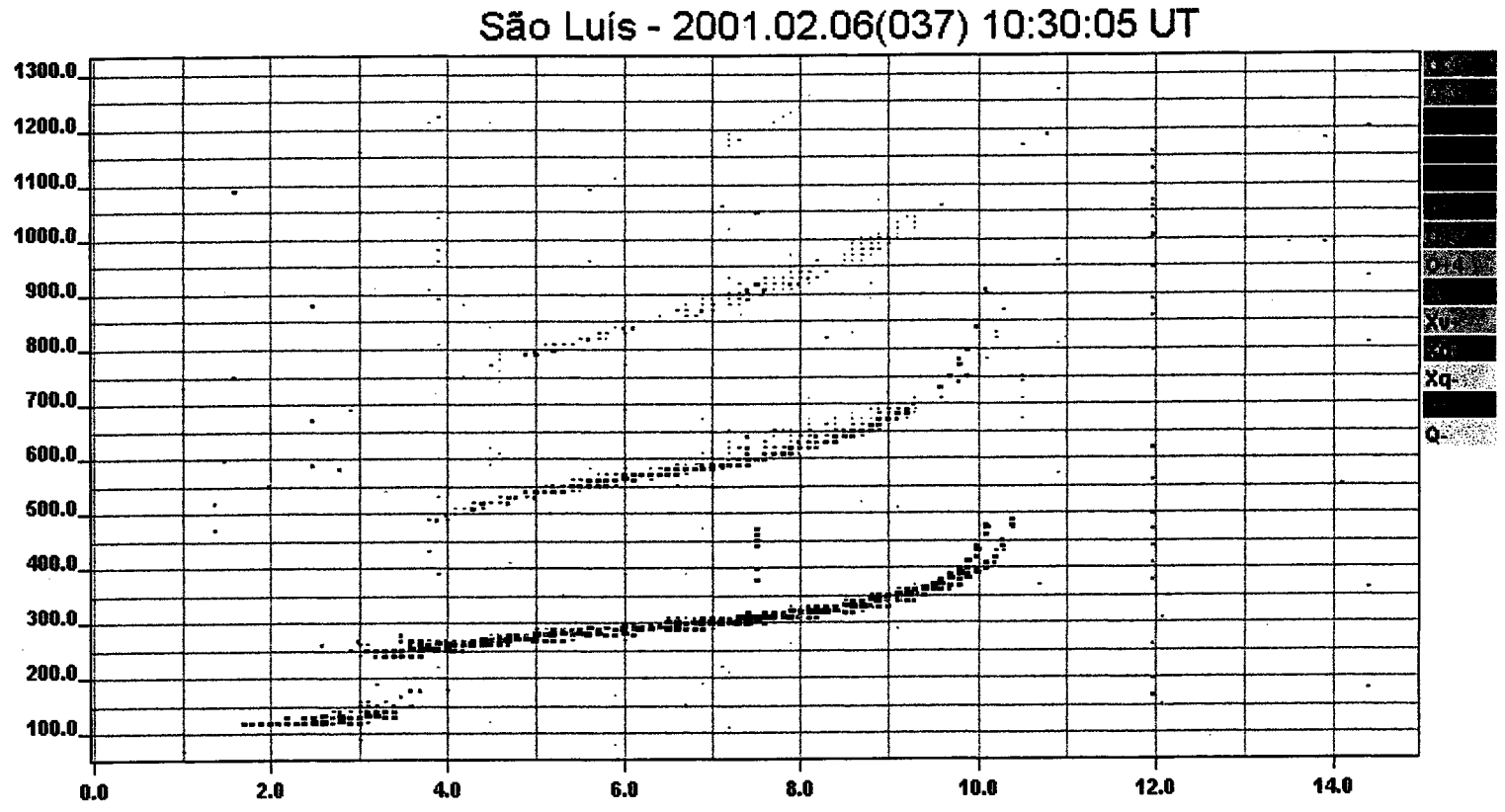
São Luís - 2001.02.06(037) 10:30:05 UT
1300.0
1200.0
1100.0
1000.0
900.0
800.0
700.0
600.0
500.0
400.0
300.0
200.0
100.0
0.0
2.0
4.0
6.0
8.0
10.0
12.0
14.0
Xq-
Q-

Fig. 06a

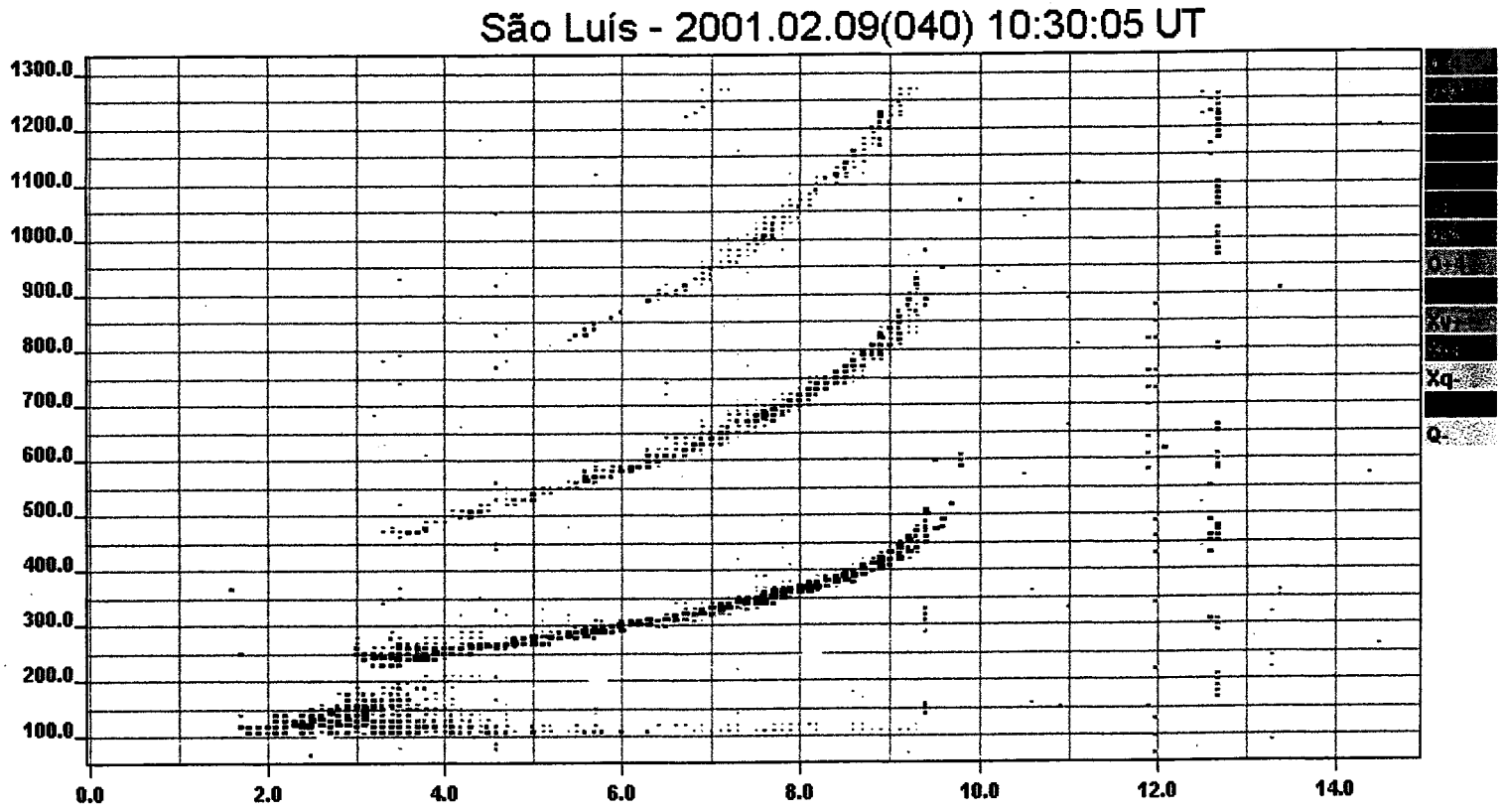
São Luís - 2001.02.09(040) 10:30:05 UT
1300.0
1200.0
1100.0
1000.0
900.0
800.0
700.0
600.0
500.0
400.0
300.0
200.0
100.0
0.0
2.0
4.0
6.0
8.0
10.0
12.0
14.0
Xq
Q

Fig. 06b

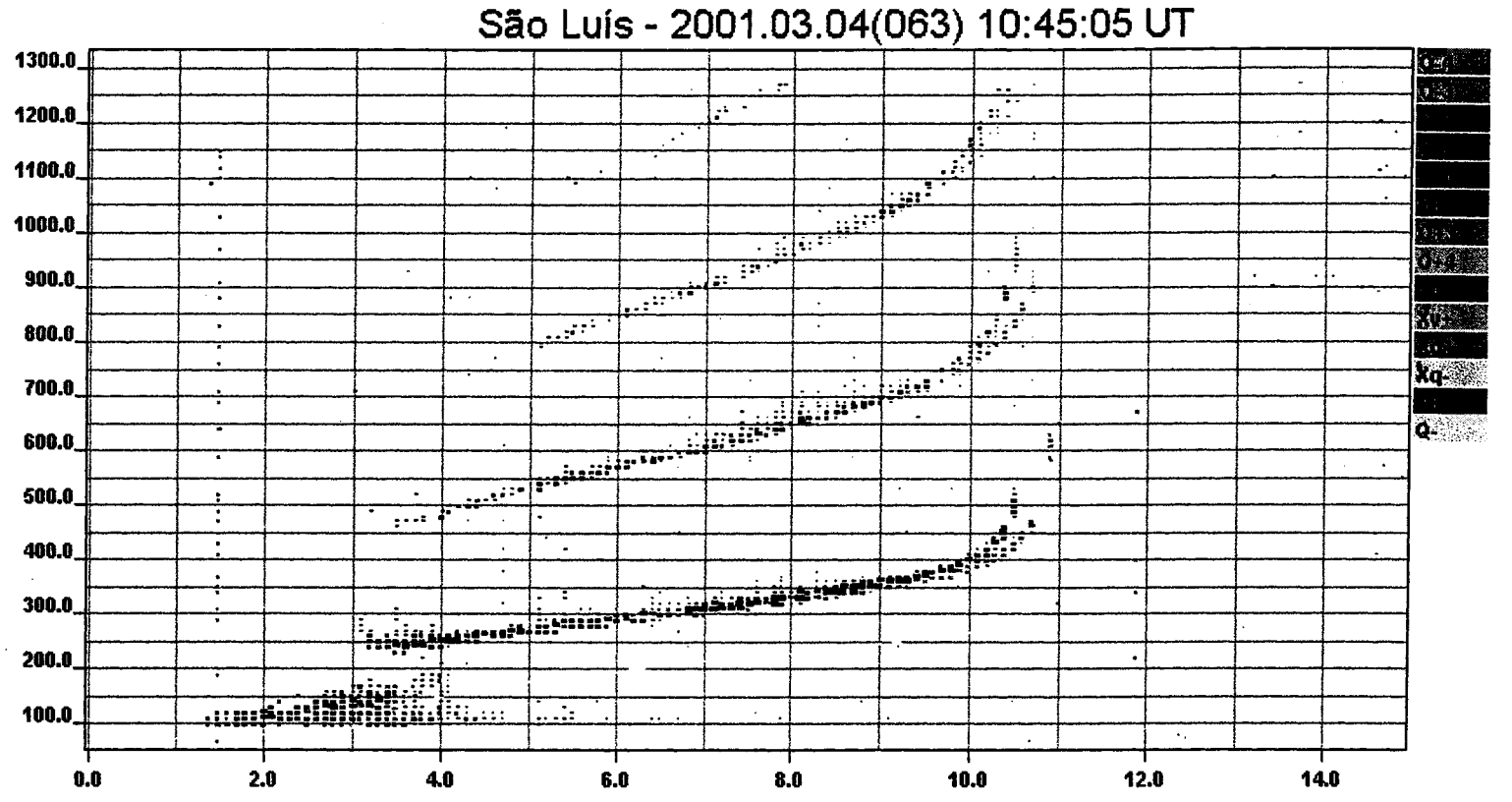
São Luís - 2001.03.04(063) 10:45:05 UT
1300.0
1200.0
1100.0
1000.0
900.0
800.0
700.0
600.0
500.0
400.0
300.0
200.0
100.0
0.0
2.0
4.0
6.0
8.0
10.0
12.0
14.0
Xq-
Q-

Fig. 06c

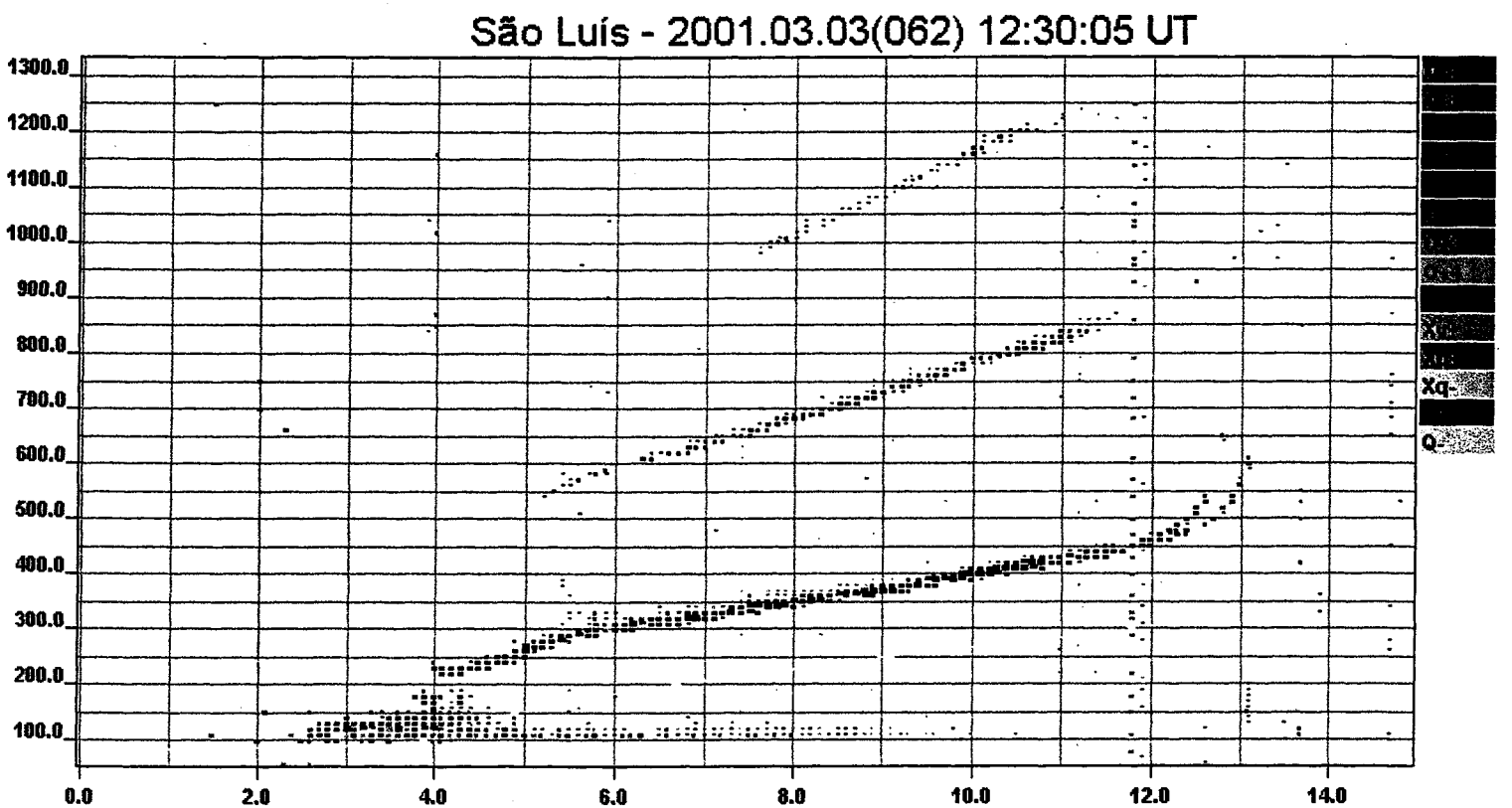
São Luís - 2001.03.03(062) 12:30:05 UT
1300.0
1200.0
1100.0
1000.0
900.0
800.0
700.0
600.0
500.0
400.0
300.0
200.0
100.0
0.0
2.0
4.0
6.0
8.0
10.0
12.0
14.0
Xq
Q

Fig. 06d

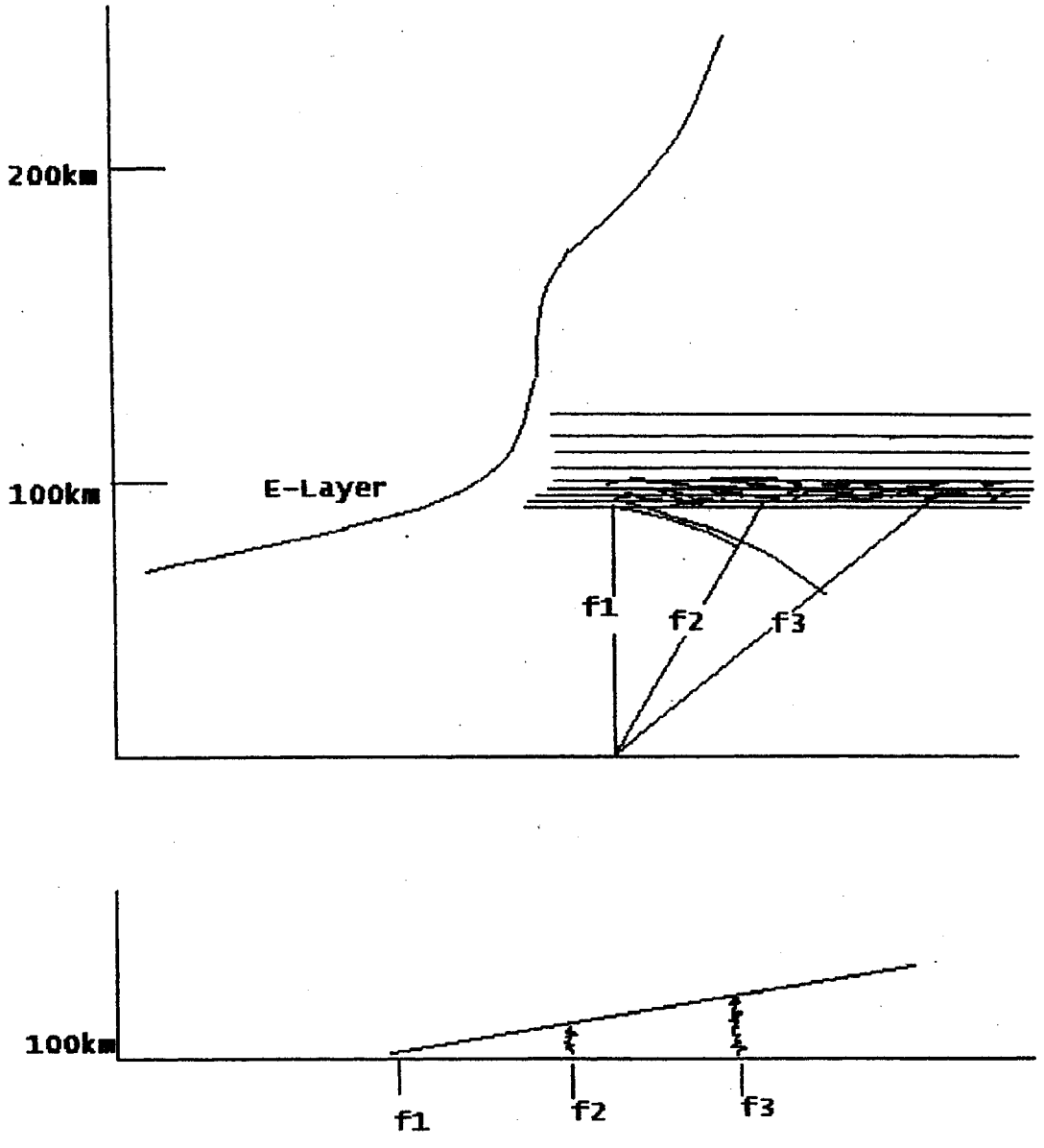

Fig. 07

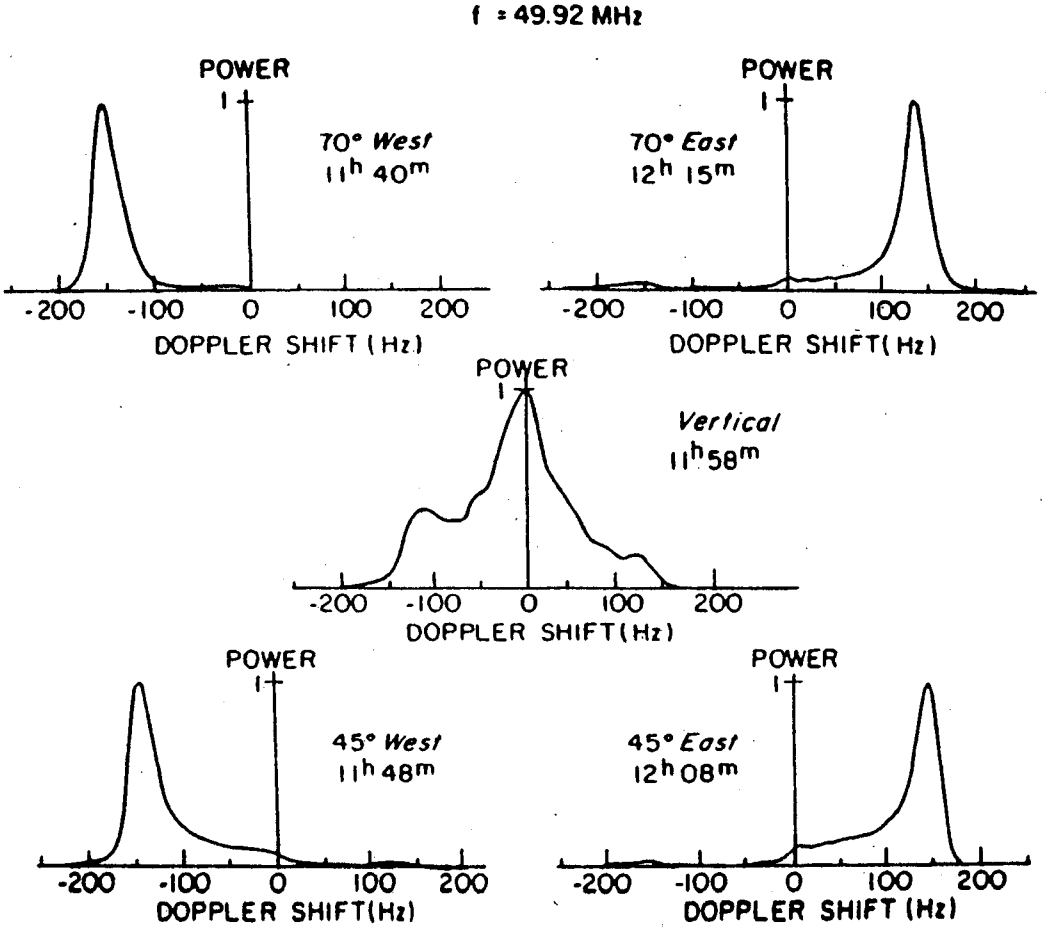

Fig. 4.20. Series of Doppler spectra from the equatorial electrojet irregularities at different elevation angles obtained at Jicamarca during a period of relatively strong scattering. The spectra are normalized to a fixed peak value. [After Cohen and Bowles (1967). Reproduced with permission of the American Geophysical Union.]

Fig. 08

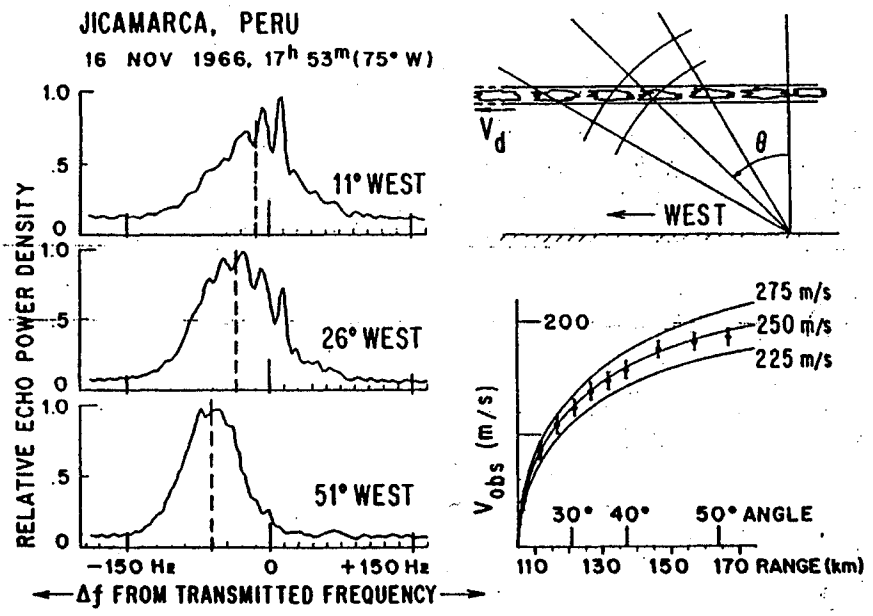

Type 2 spectra measured at 50 MHz simultaneously at different antenna zenith angles. The dashed lines indicate the average Doppler shifts. The geometry of the experiment is shown in the top right-hand panel. The results of the experiment, together with three theoretical curves for which a sine dependence of the average phase velocity with zenith angle was assumed, are shown in the bottom right-hand panel [after *Balsley*, 1969].

Fig. 09

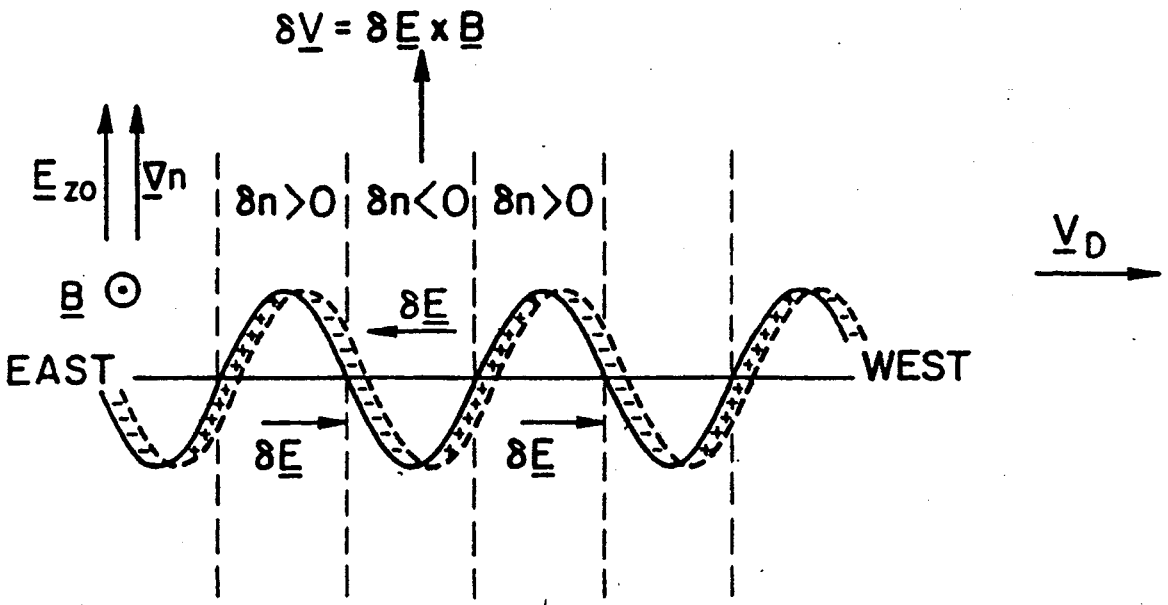

Schematic diagrams showing the gradient drift process for daytime conditions.

Fig. 10

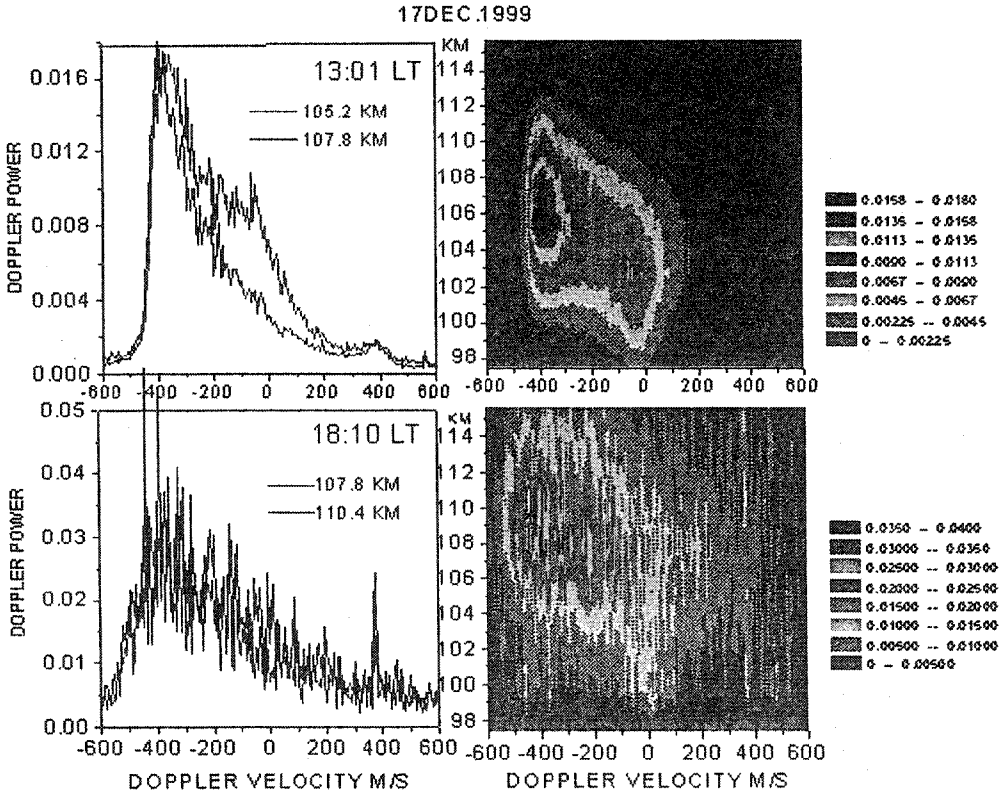
17DEC.1999
13:01 LT
105.2 KM
107.8 KM
DOPPLER POWER
KM
18:10 LT
107.8 KM
110.4 KM
DOPPLER POWER
DOPPLER VELOCITY M/S
DOPPLER VELOCITY M/S

Fig. 11

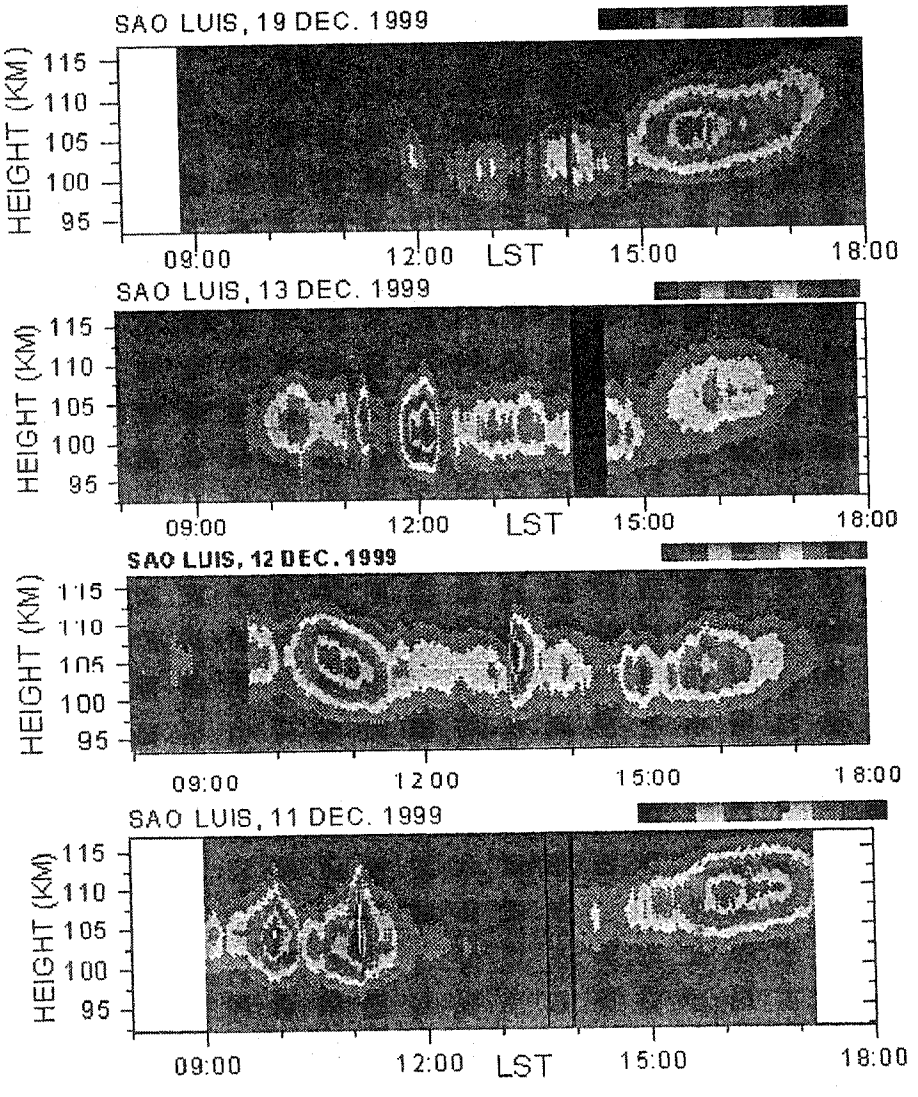
SAO LUIS, 19 DEC. 1999
HEIGHT (KM)
115
110
105
100
95
09:00
12:00
LST
15:00
18:00
SAO LUIS, 13 DEC. 1999
HEIGHT (KM)
115
110
105
100
95
09:00
12:00
LST
15:00
18:00
SAO LUIS, 12 DEC. 1999
HEIGHT (KM)
115
110
105
100
95
09:00
12:00
15:00
18:00
SAO LUIS, 11 DEC. 1999
HEIGHT (KM)
115
110
105
100
95
09:00
12:00
LST
15:00
18:00

Fig. 12a

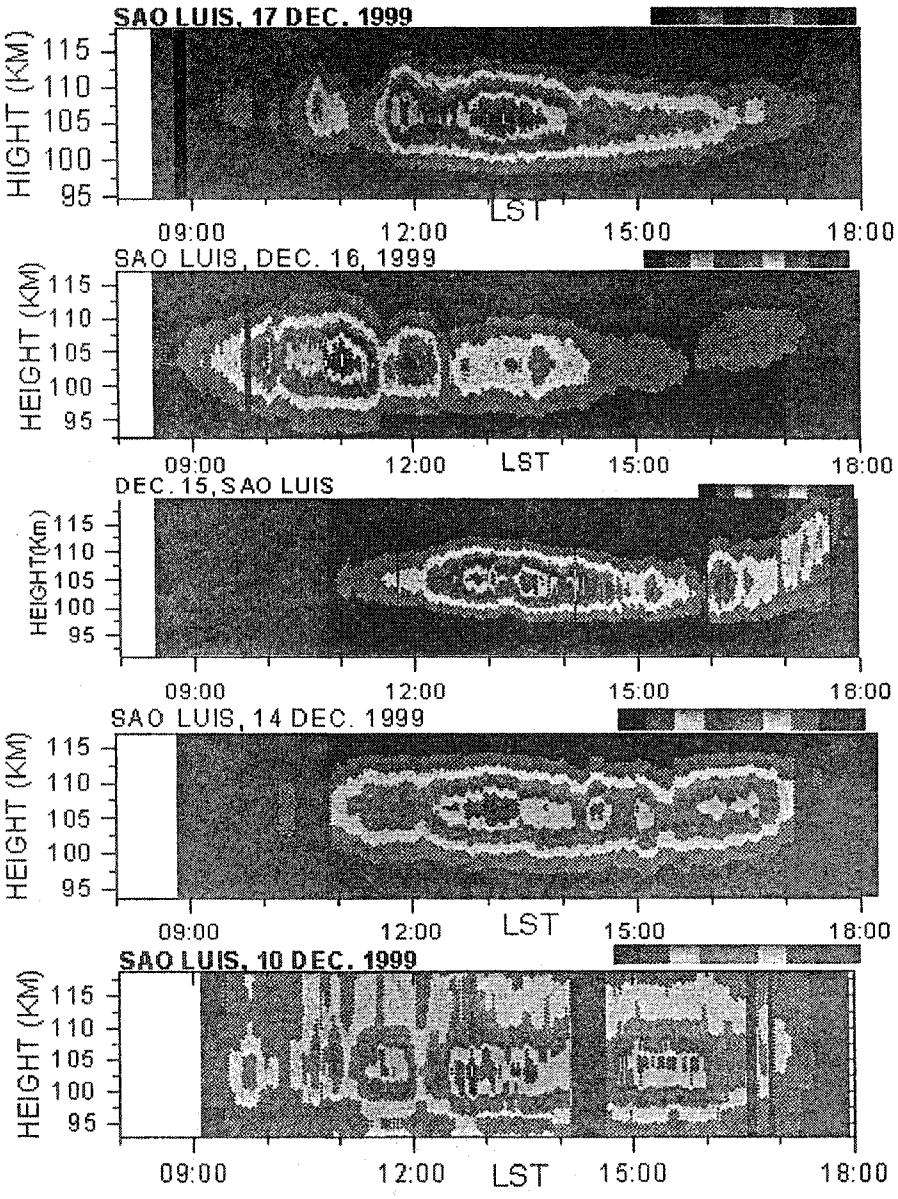
SAO LUIS, 17 DEC. 1999
HIGHT (KM)
115
110
105
100
95
09:00
12:00
LST
15:00
18:00
SAO LUIS, DEC. 16, 1999
HEIGHT (KM)
DEC. 15, SAO LUIS
HEIGHT(Km)
SAO LUIS, 14 DEC. 1999
SAO LUIS, 10 DEC. 1999

Fig. 12b

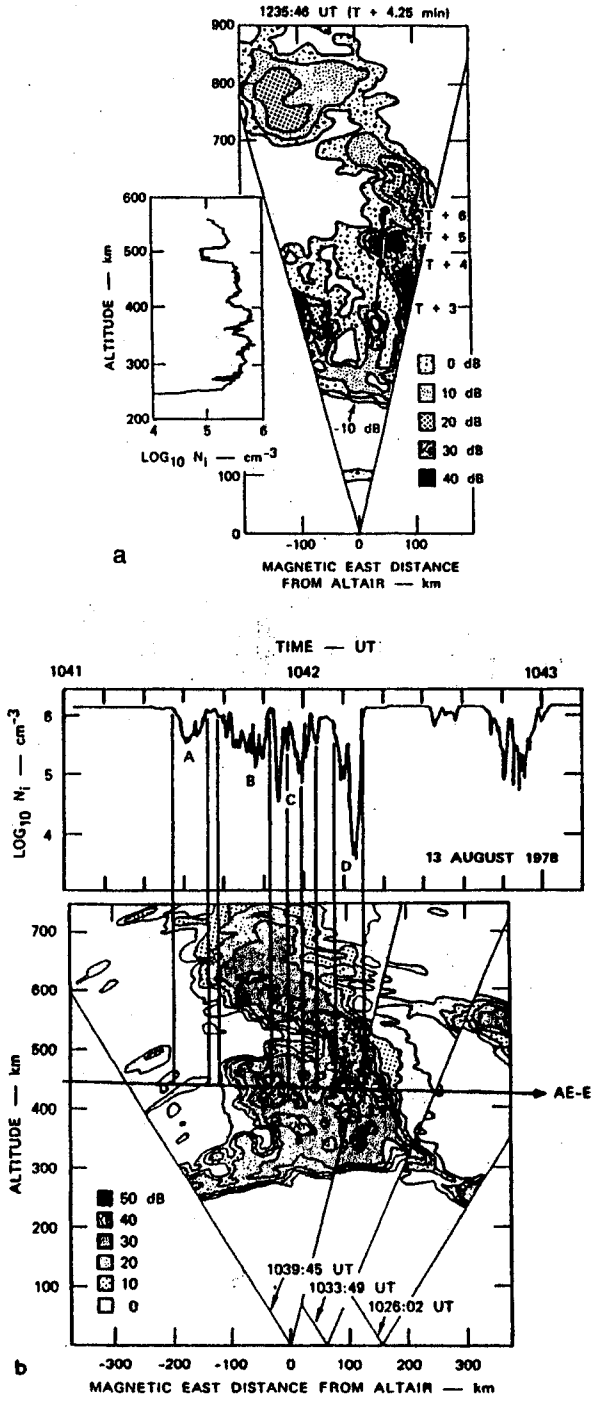

(a) Simultaneous vertical rocket plasma density profile and backscatter map made with the Altair radar on the island of Kwajalein. Dots show the rocket trajectory. [After Rino *et al.* (1981). - Reproduced with permission of the American Geophysical Union.] (b) Simultaneous horizontal satellite plasma density profile and backscatter map made with the Altair radar. [After Tsunoda *et al.* (1982). Reproduced with permission of the American Geophysical Union.]

Fig. 13

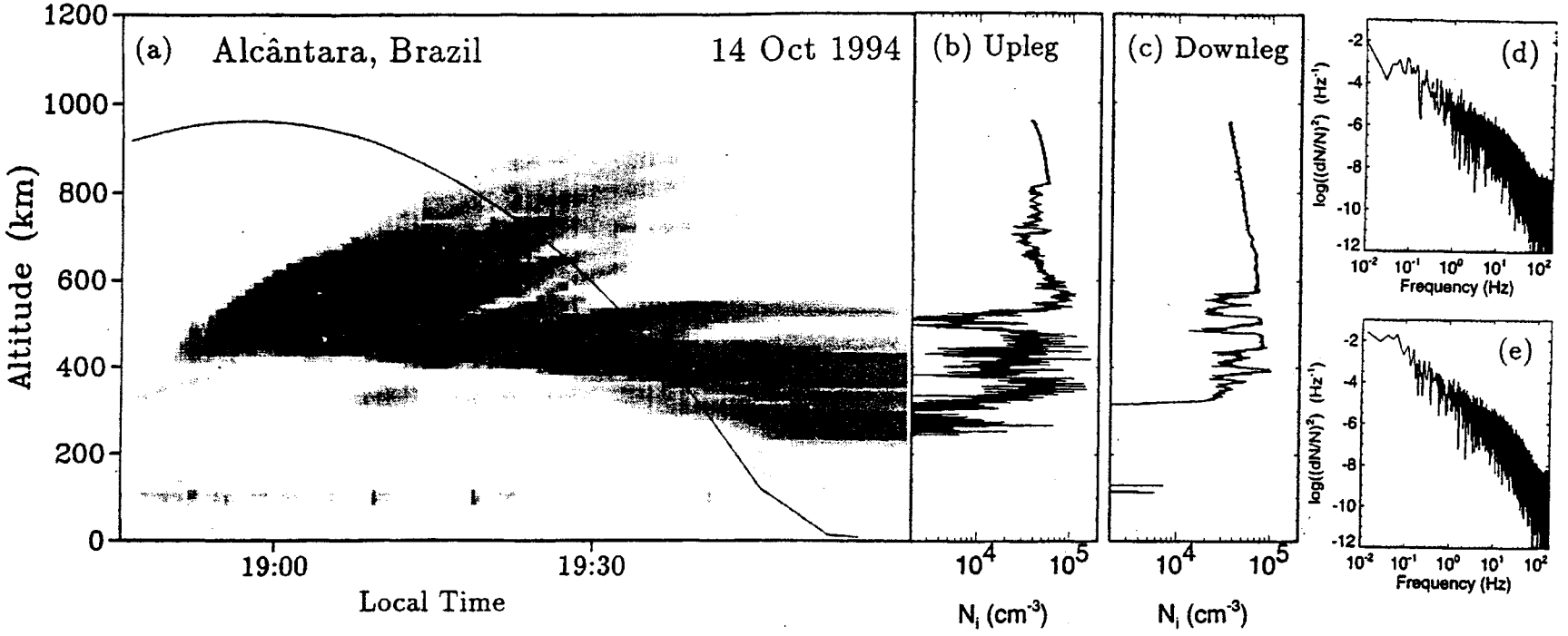

A comparison of radar and rocket data: (a) the CUPRI RTI for 1845–2000 LT on October 14; (b) the electron density profile measured with the Langmuir probe during the upleg portion of the rocket flight; (c) the correponding profile for the downleg; and spectra of density irregularities at (d) 600-800 km on the upleg and (e) 400-600 km on the downleg. The solid line in (a) shows an estimated rocket trajectory through the ESF structures detected by the radar.

Fig. 14

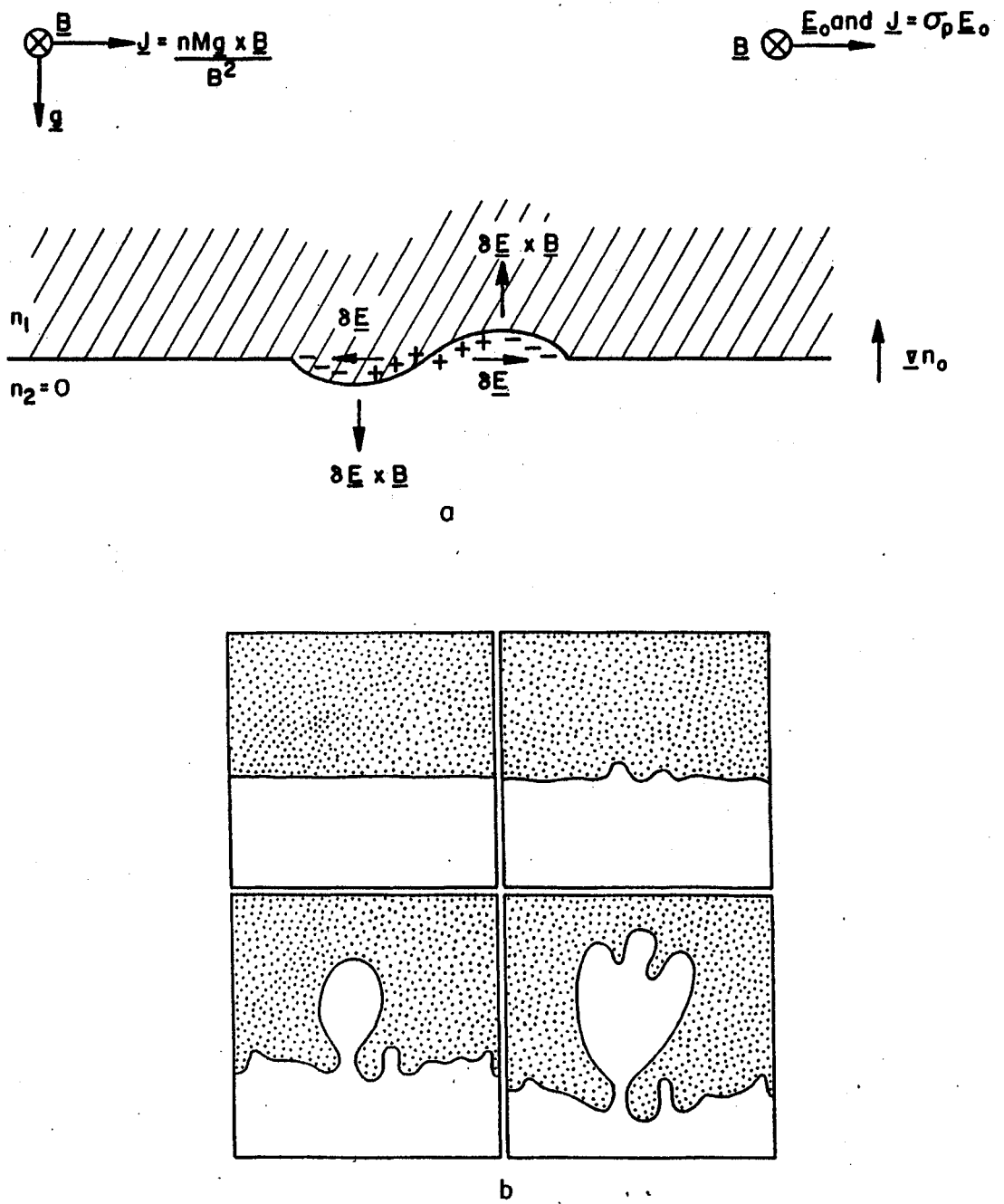

(a) Schematic diagram of the plasma analog of the Rayleigh–Taylor instability in the equatorial geometry. (b) Sequential sketches made from photos of the hydrodynamic Rayleigh–Taylor instability. A heavy fluid is initially supported by a transparent lighter fluid.

Fig. 15

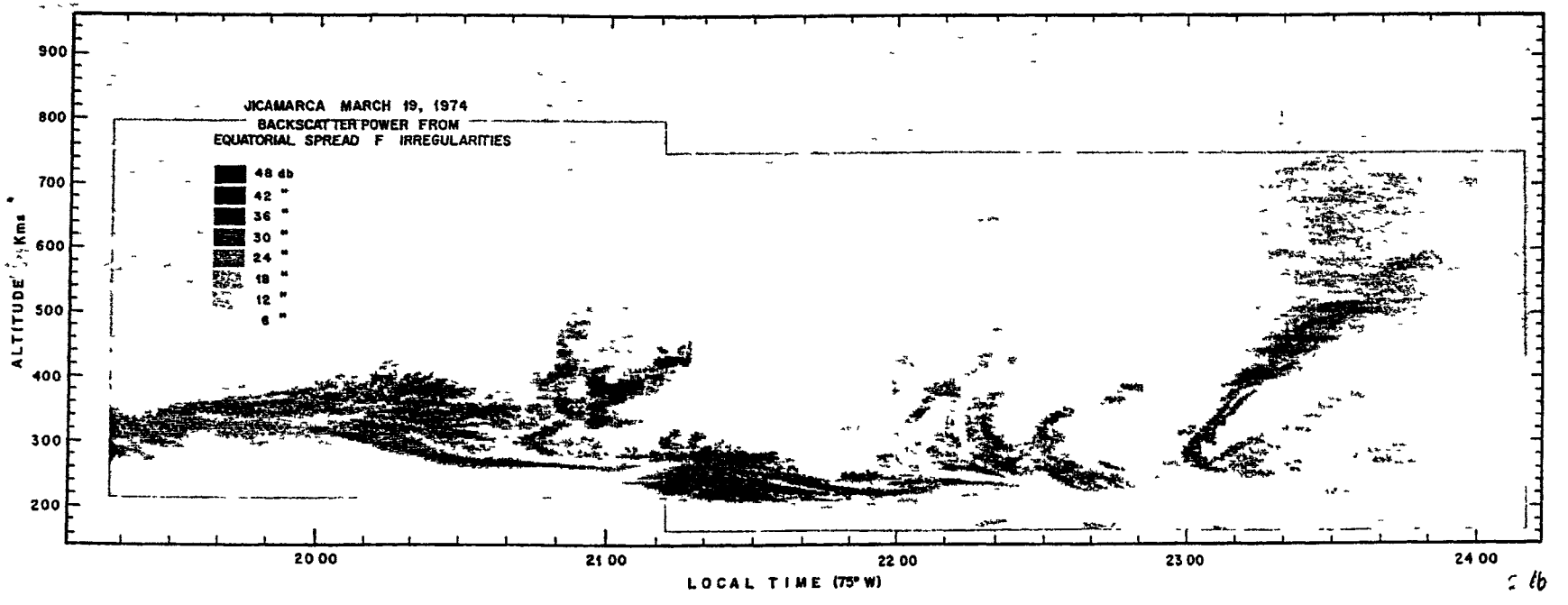
JICAMARCA MARCH 19, 1974
BACKSCATTER POWER FROM
EQUATORIAL SPREAD F IRREGULARITIES
48 db
42 "
36 "
30 "
24 "
18 "
12 "
6 "
ALTITUDE (Kms)
900
800
700
600
500
400
300
200
20 00
21 00
22 00
23 00
24 00
LOCAL TIME (75° W)

Fig 16

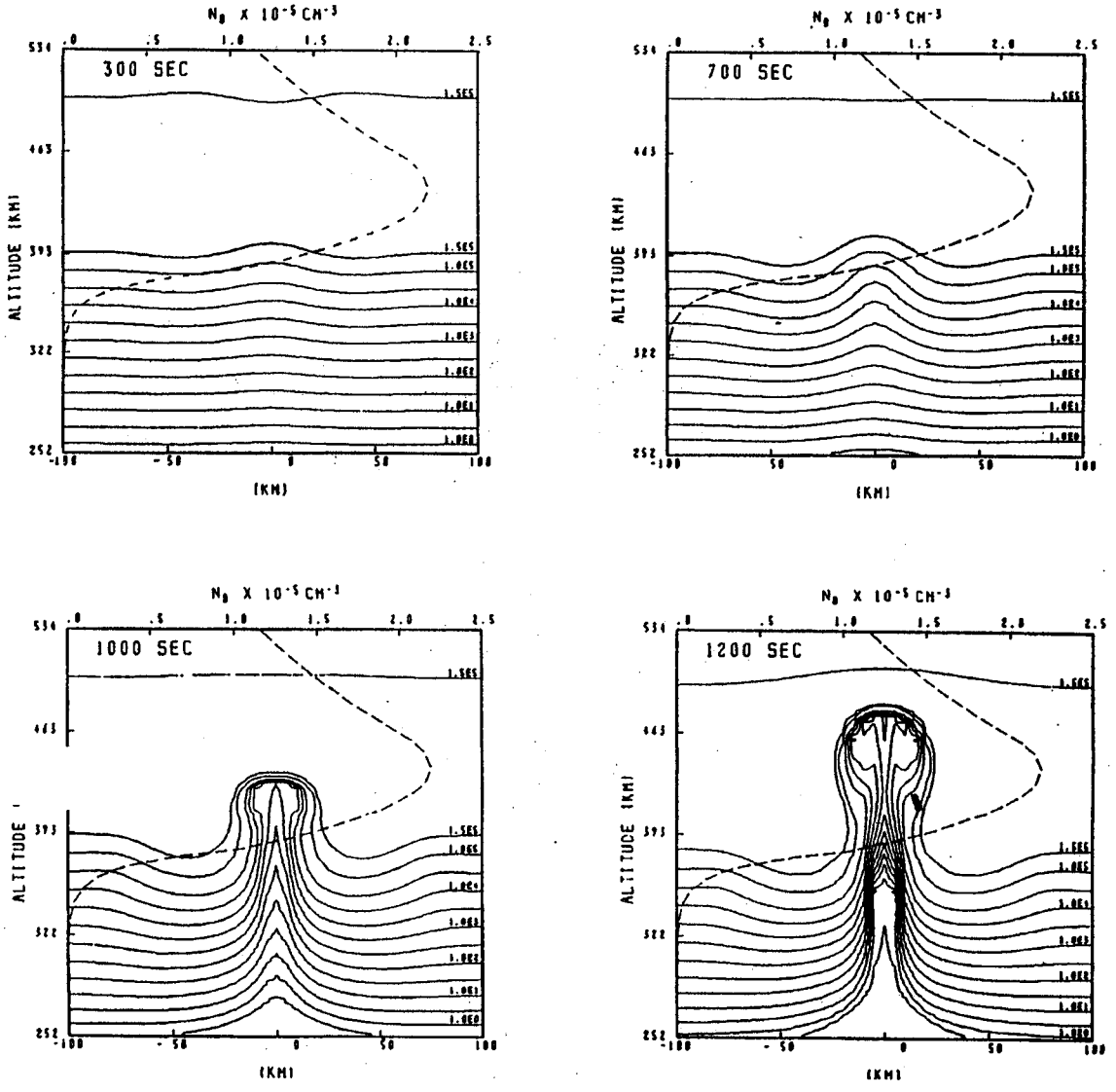

Fig. 17a

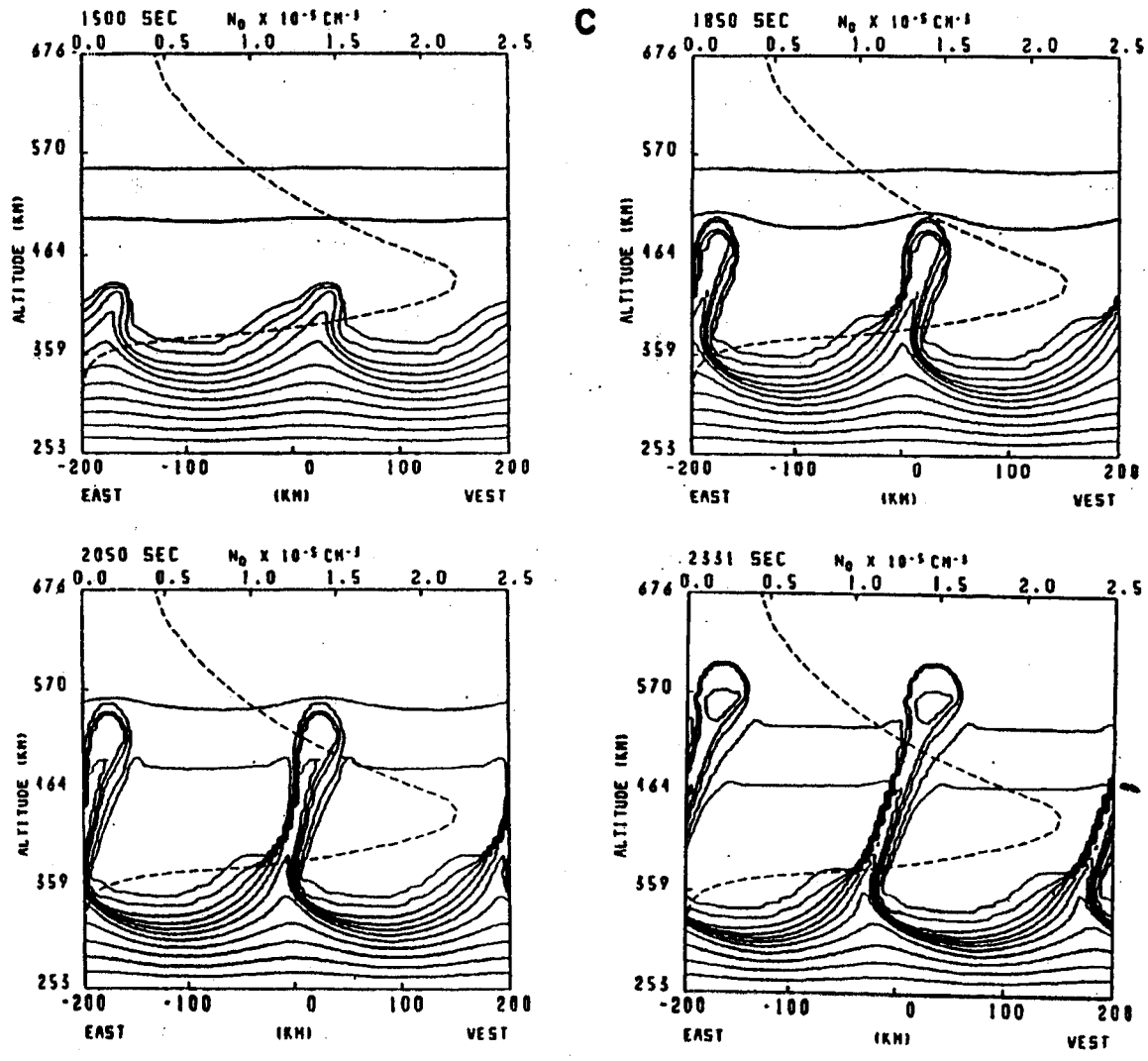
C
1500 SEC
1850 SEC
2050 SEC
2331 SEC
0.0 0.5 1.0 1.5 2.0 2.5
676
570
464
359
253
ALTITUDE (KM)
-200 -100 0 100 200
EAST
(KM)
VEST

Fig. 17b

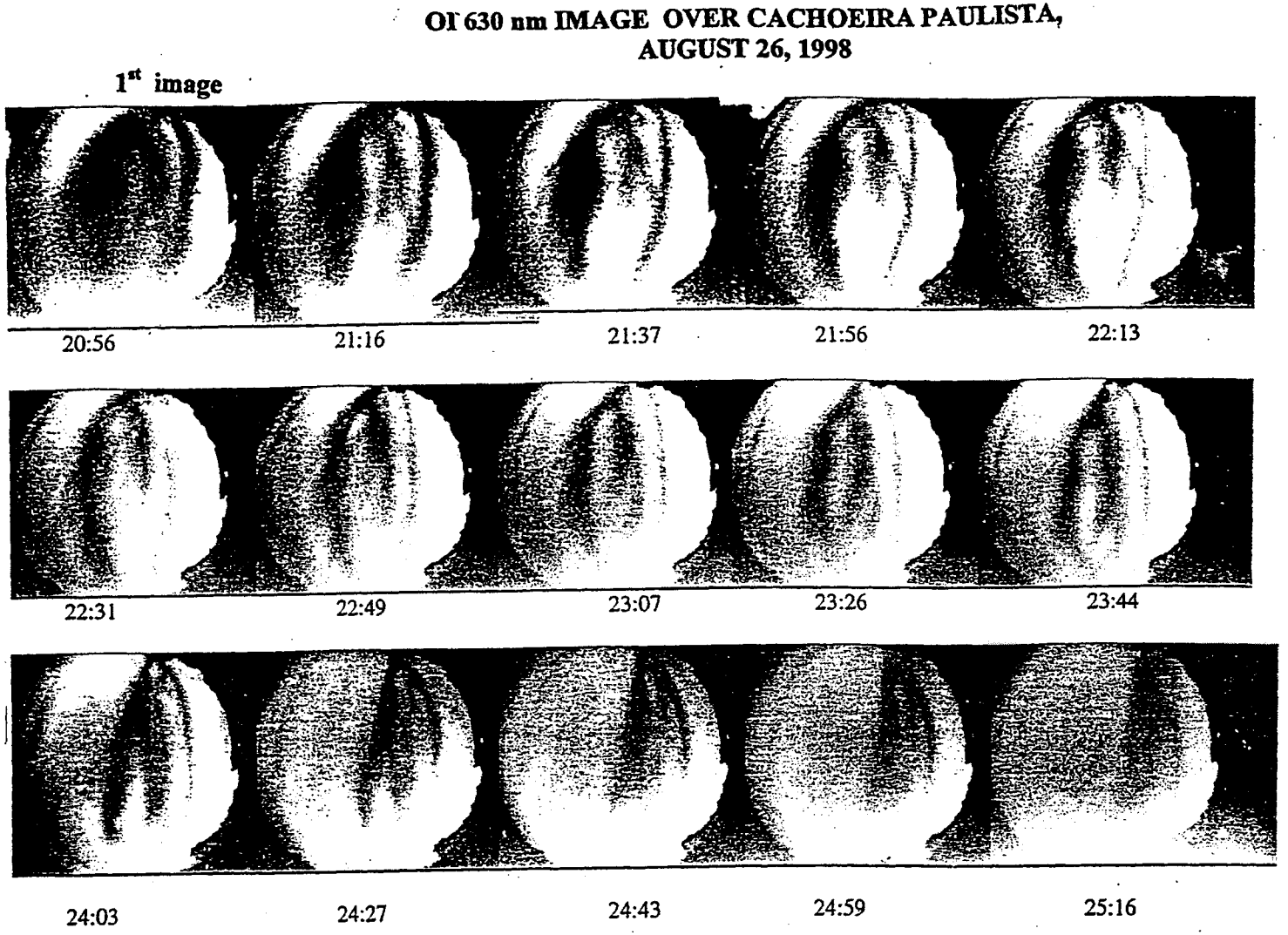
OI 630 nm IMAGE OVER CACHOEIRA PAULISTA,
AUGUST 26, 1998
1st image
20:56
21:16
21:37
21:56
22:13
22:31
22:49
23:07
23:26
23:44
24:03
24:27
24:43
24:59
25:16
LOCAL TIME

Fig. 18a

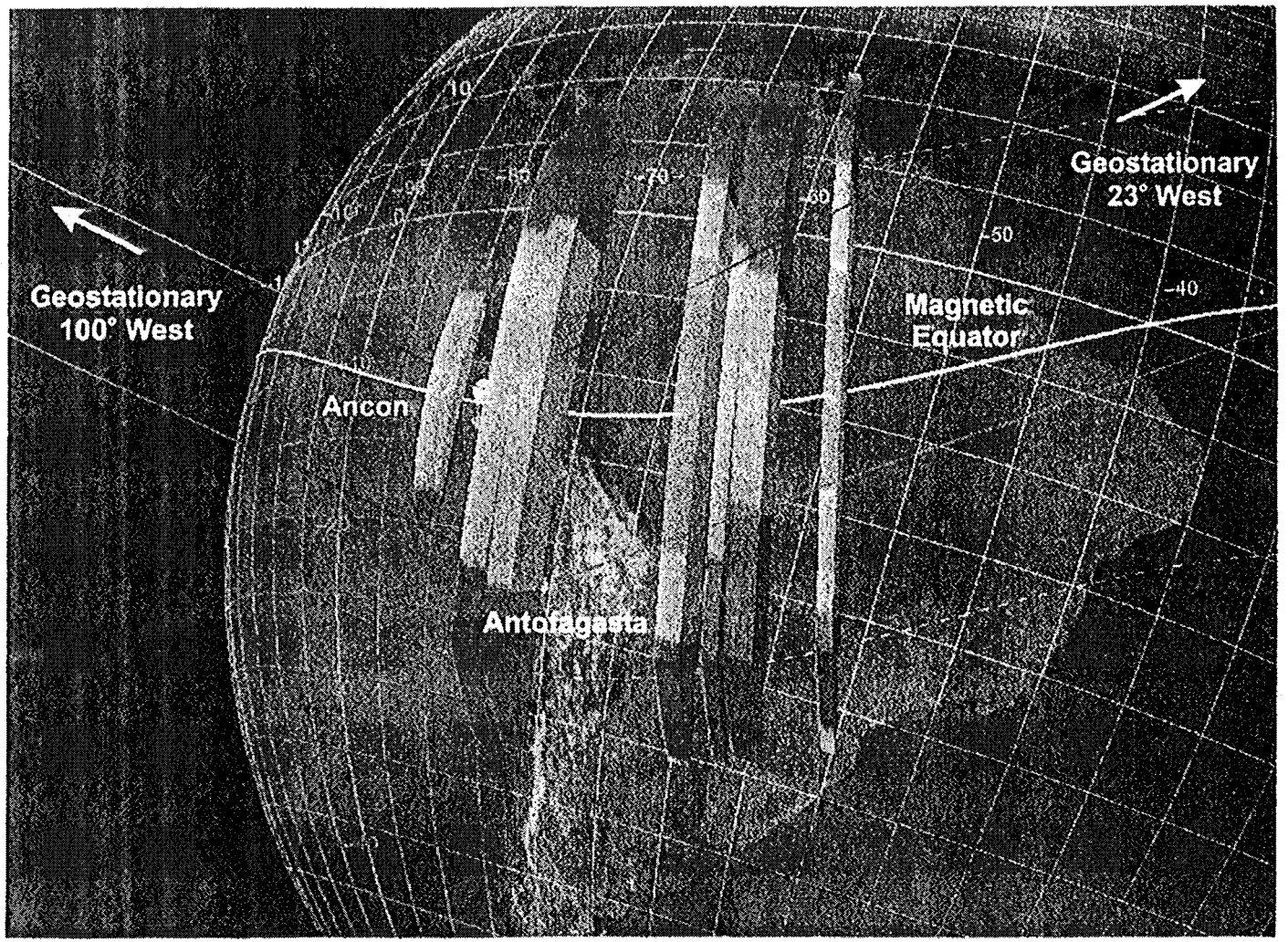

Plate 1a. Three-dimensional visualization of equatorial scintillation bubbles observed by SCINDA in October 1996. The system updates the visualization dynamically four times per hour. Bubble amplitude, location, growth, and decay are determined by an empirical model driven by real-time observations of scintillation intensity and zonal drift. Ray paths from the observing stations at Ancon and Antofagasta to geostationary satellites at 100 W and 23 W are color-coded red when they are scintillating and green when they are unperturbed.

Fig. 18b

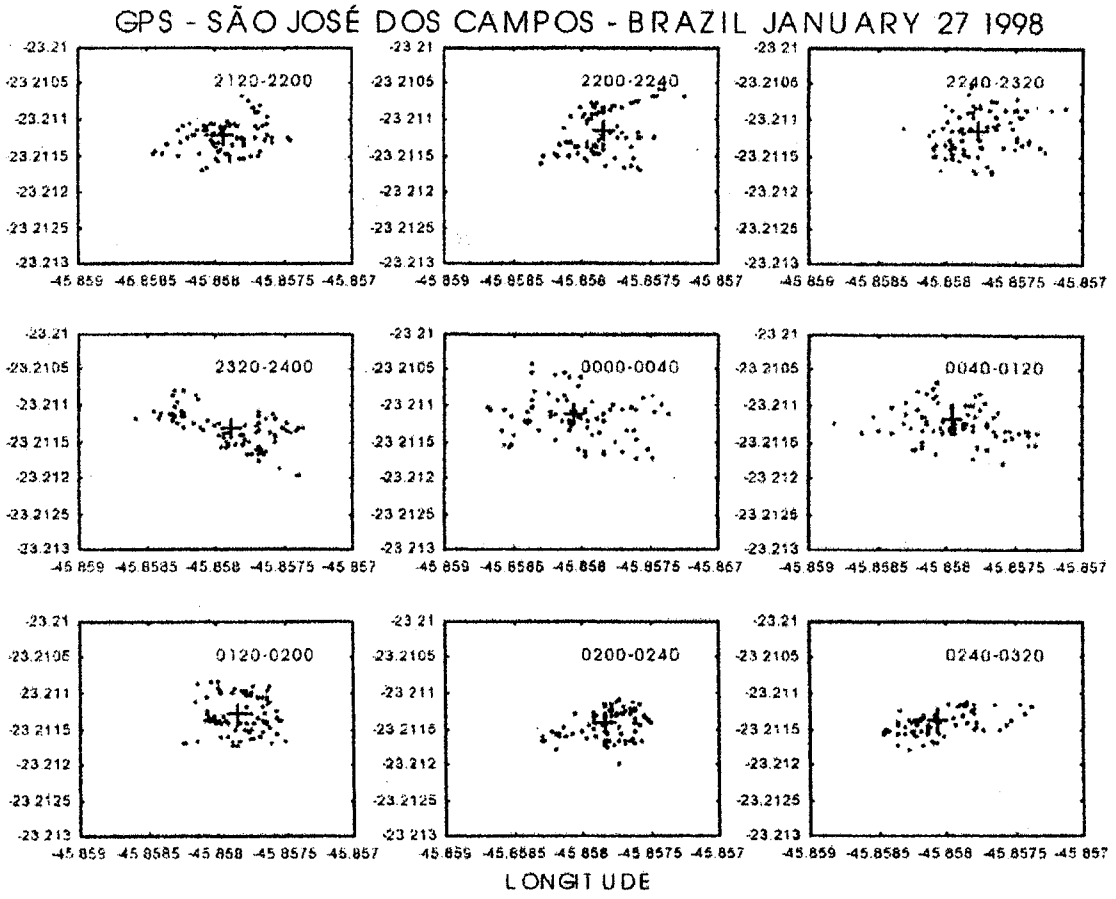
GPS - SÃO JOSÉ DOS CAMPOS - BRAZIL JANUARY 27 1998
2120-2200
2200-2240
2240-2320
2320-2400
0000-0040
0040-0120
0120-0200
0200-0240
0240-0320
LONGITUDE

Fig. 19